

**Dark Shower Investigations at Belle II for Strongly
Interacting Dark Sectors**

by

Tim Tueschen

A THESIS SUBMITTED IN PARTIAL FULFILLMENT
OF THE REQUIREMENTS FOR THE DEGREE OF

Master of Science

in

THE FACULTY OF GRADUATE AND POSTDOCTORAL
STUDIES

(Physics)

The University of British Columbia

(Vancouver)

October 2022

© Tim Tueschen, 2022

The following individuals certify that they have read, and recommend to the Faculty of Graduate and Postdoctoral Studies for acceptance, the thesis entitled:

Dark Shower Investigations at Belle II for Strongly Interacting Dark Sectors

submitted by **Tim Tueschen** in partial fulfillment of the requirements for the degree of **Master of Science in Physics**.

Examining Committee:

Janis McKenna, Professor, Physics and Astronomy, UBC
Supervisor

Chris Hearty, Professor, Physics and Astronomy, UBC
Supervisory Committee Member

Abstract

The so far unresolved question of the nature of dark matter has led to the development of a multitude of particle physics models that all meet current experimental and theoretical constraints, but differ greatly in the experimental signatures they predict. One idea that has been gaining popularity is that there could be a whole family of dark matter particles, forming a so called 'dark sector' that interacts only very feebly with regular matter. In this thesis we investigate a hypothetical strongly interacting dark sector that confines at the GeV scale, which results in the production of a shower of dark sector mesons, including a long-lived neutral particle. This would result in a displaced vertex signature at e^+e^- colliders such as the Belle II experiment. We provide a brief overview of current evidence for Dark Matter and existing constraints to motivate the choice of a QCD-like dark sector with a dark photon mediator, as well as a detailed description of the Belle II detector which has an excellent sensitivity to displaced vertex signatures. After briefly summarizing the model, we describe the general search strategy, examine possible sources of background, and test the feasibility of a zero-background analysis. We find that, while not all signatures can be investigated in the zero-background case, the model offers a large parameter space that can be well investigated at Belle II with currently available data.

Lay Summary

We know from a range of experiments that there is a mismatch between the amount of matter we can see, and so the amount of mass we can measure, compared to what our laws of gravity predict. This leads to the theory that one or more particles exist that can interact through gravity but do not interact frequently with light or regular matter. Because of its infrequent interactions, this supposed Dark Matter is difficult to detect, let alone measure, but we are able to put some constraints on properties such as its interaction strength and its relative abundance. In this thesis we investigate a particular model of Dark Matter and discuss strategies of how we can search for the unique experimental signature it predicts. We find that current particle physics experiments such as Belle II are well suited for this kind of investigation and predict promising results in the future.

Table of Contents

Abstract	iii
Lay Summary	iv
Table of Contents	v
List of Tables	vii
List of Figures	viii
Glossary	x
Acknowledgments	xii
1 Introduction	1
1.1 Evidence for Dark Matter	2
1.2 Properties of Dark Matter	4
1.3 Dark Sectors	4
1.4 Search Strategies	6
2 Belle II Experiment	7
2.1 Improvements over Belle	7
2.2 Beams	8
2.3 Interaction Point	9
2.4 Pixel Detector	9
2.5 Silicon Strip Detector	11

2.6	Drift Chamber	13
2.7	Particle Identification	14
2.8	Electromagnetic Calorimeter	15
2.9	K_{long} and Muon Detector	16
2.10	Software	17
2.11	Trigger	17
	2.11.1 Level 1 Trigger	18
	2.11.2 Higher Level Trigger	19
3	Theory	21
3.1	Lagrangian construction	21
3.2	Relic Density	24
3.3	Parameter Space	25
4	Analysis Structure and Event Selection	27
4.1	Signal Generation	28
4.2	Background	29
4.3	Background Separation	32
4.4	Discriminating Variables	35
4.5	Trigger Efficiency	37
5	Analysis	45
6	Conclusion and Outlook	54
	Bibliography	56
A	Appendix	59

List of Tables

Table 4.1	Overall selection criteria	36
Table 4.2	Selection criteria dependent on vertex location	36
Table A.1	Summary of the Belle II detector components	60

List of Figures

Figure 1.1	Composite image of Bullet Cluster	3
Figure 2.1	Schematic of the full Belle II Detector	8
Figure 2.2	Image of the Belle II Pixel Detector	10
Figure 2.3	Image of the Belle II Silicon Vertex Detector	12
Figure 2.4	Schematic of the Belle II Drift Chamber	13
Figure 2.5	Design and function of the Time of Propagation counter . . .	14
Figure 2.6	Schematic of the Belle II ECL and detailed crystal layout . . .	16
Figure 3.1	Illustration of a Dark Shower Event	22
Figure 3.2	Available parameter space for Λ	26
Figure 4.1	ρ_d^0 multiplicity as a function of mass	27
Figure 4.2	ρ_d^0 branching ratios as a function of mass	30
Figure 4.3	Backgrounds in Region 1	33
Figure 4.4	Backgrounds in Region 2	33
Figure 4.5	Backgrounds in Region 3	33
Figure 4.6	Figure of Merit example	34
Figure 4.7	Signal selection efficiency	39
Figure 4.8	Plot of muonID for background and example signal	40
Figure 4.9	Showcase of reflected peaks due to misidentified pions	40
Figure 4.10	Plot of $\cos(\text{PV angle})$ for background and example signal . . .	41
Figure 4.11	Plot of $\cos(\eta)$ for background and example signal	41
Figure 4.12	Overall efficiency of the L1 trigger	42
Figure 4.13	Detailed L1 trigger efficiencies	43

Figure 4.14	HLT efficiency after L1 Triggers have been applied.	44
Figure 5.1	Number of events after selection cuts	46
Figure 5.2	Number of events after selection cuts and scaling	47
Figure 5.3	Example double sided Crystal Ball fits	48
Figure 5.4	Reduced χ^2 values for each individual Crystal Ball fit.	49
Figure 5.5	Uncertainty in the reconstructed mass	49
Figure 5.6	Mean and std for mass pulls	50
Figure 5.7	Fit results for the shape parameters	51
Figure 5.8	Sigma and FWHM for Crystal Ball fits	52
Figure 5.9	Exclusion bounds for 2 track mu channel analysis	53
Figure 5.10	Projected exclusion bounds for full analysis	53

Glossary

ARICH Aerogel Ring Imaging Cherenkov detector

ASICS application-specific integrated circuits

BASF2 Belle II Analysis Software Framework

CDC Central Drift Chamber , a large array of wires used for tracking

CM center-of-mass

CP Charge-Parity, a type of symmetry in physics

DM Dark Matter , a hypothetical form of matter thought to account for approximately 85% of the matter in the universe

ECL Electromagnetic Calorimeter , used to measure energy depositions

KLM K_{long} and Muon Detector , the outermost detector part

LHC Large Hadron Collider

LLP long-lived particle

MC Monte Carlo

PXD Pixel Detector , innermost part of the detector

QCD Quantum Chromodynamics

SM Standard Model , of particle physics describes all known elementary particles

SVD Silicon Vertex Detector , surrounds the PXD

TOP Time of Propagationcounter

VXD Vertex Detector , consisting of PXD and SVD

Acknowledgments

First and foremost, I have to thank Prof. Janis McKenna and Prof. Chris Hearty, not only for the opportunity to work as part of the Belle II group, but for their invaluable advice, support, and patience during my degree.

Many thanks also to Miho, Michael and Daniel for their constant insightful feedback and answering my many questions. It really was a joy to work together and see all of you in the office day-to-day.

Thanks also to Ryan and Gaurav for proof-reading and helpful comments.

Chapter 1

Introduction

The Standard Model (SM) of particle physics is thus far one of the most rigorously tested scientific theories and has been incredibly successful at describing fundamental particles and their interactions, at least at currently achievable energies and experimental precision. It is generally formulated as a perturbatively renormalizable quantum field theory which describes three of the four fundamental forces of nature: the strong force, the weak force, and the electromagnetic force, with gravity being the notable omission. Despite its unparalleled success the Standard Model leaves important gaps, not just in relation to gravity but also including but not limited to the issues of Neutrino Mass, Charge-Parity (CP) violation in the Quantum Chromodynamics (QCD) sector, matter-antimatter asymmetry, Dark Energy and Dark Matter. Of these issues the search for a Dark Matter (DM) candidate is especially interesting since theoretical models are strongly limited by existing cosmological and astrophysical observations while the predicted potential Dark Matter particles may be largely accessible in existing particle physics experiments. This means we can make strong predictions about a given model's phenomenology and can immediately apply them to search strategies for datasets that are either currently available or will be in the near future.

1.1 Evidence for Dark Matter

The existence of Dark Matter is on firm theoretical ground with evidence for it coming from multiple different observations. The four most commonly cited ones are briefly explained below while a more extensive list can be found in reference [22].

1. The most well-known evidence comes from the observation of galaxy rotations. We can measure the orbital speed of luminous matter, i.e. stars and gas, in spiral galaxies and see a noticeable discrepancy between our observations and what we would predict based on Newton's law of gravity. We know that the gravitational force must be, at least approximately, equal to the centrifugal force. As the density of visible matter decreases we expect the orbital speed to drop as $\frac{1}{\sqrt{r}}$ where r is the orbital distance, but observations of many spiral galaxies show that their orbital speed approaches a constant value. To resolve this discrepancy while retaining Newton's law of gravity it is hypothesized that there must be a large sphere of Dark Matter around (most) galaxies. This was first noted by Vera Rubin and Kent Ford [23].
2. Similarly, an analysis of galaxy clusters provides evidence through the virial theorem. The virial theorem lets us relate the total kinetic energy of a stable system of discrete particles to the total potential energy of the system, which applied to galaxy clusters lets us relate the total mass contained in the cluster to the average speed at which individual galaxies move. Fritz Zwicky was the first to note that, when applied to the Coma cluster, the virial theorem predicts its total mass to be magnitudes larger than the detectable luminous mass, which points to the existence of a large amount of non-luminous, i.e. dark, matter [30]. Later analyses significantly revised the results but the conclusion remains the same [6].
3. Gravitational lensing, i.e. the fact that the path of light is bent by mass between the source and the observer, is another mechanism that provides evidence for Dark Matter. Most famously, we can define the center of mass the two colliding subclusters that make up the Bullet Cluster, shown in Figure 1.1, and compare it to the center of mass as measured through gravitational

lensing. We see that these two centers are displaced from another, which can be explained if the clusters contain a large amount of non or only weakly interacting Dark Matter while the visible matter is slowed through electromagnetic interactions [9].

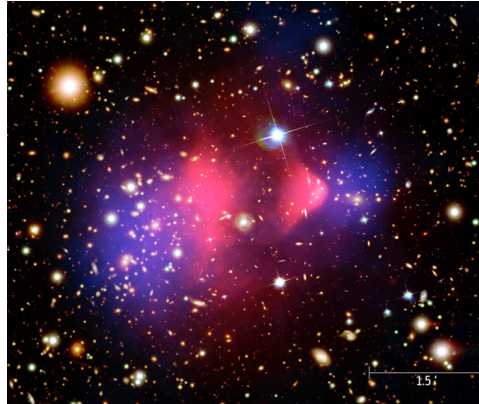


Figure 1.1: The composite image shows galaxy cluster 1E 0657-56, also known as the "Bullet Cluster". Hot gas is shown in pink while the blue areas show the mass concentration as determined using gravitational lensing. Most of the mass is visibly separate from the normal matter, providing evidence that the matter in the cluster is dark [29].

4. Lastly we can quantify the amount of Dark Matter in our universe from measurements of the cosmic microwave background. The Cosmic Microwave Background (CMB) is a remnant from cosmic recombination, when electrons combined with nuclei, decoupling the photons and making the universe transparent. The resulting radiation almost resembles an ideal black body with a temperature of 2.7K with only incredibly small fluctuations. These anisotropies were measured by a series of satellite missions, most recently by the Planck satellite. We can relate their power spectrum to the acoustic oscillations of the baryon-photon fluid, which lets us measure the relative baryon and Dark Matter densities [2].

1.2 Properties of Dark Matter

Before delving into the details of particle Dark Matter, it is necessary to mention that these pieces of evidence can also be explained by other theories, for example by modifying the law of gravity. Some relativistic theories of modified gravity can successfully explain flat rotation curves and observations from structure formation but fail to address the CMB power spectrum [11]. However, particle Dark Matter has the ability to match all observations through the sheer wealth of possible interactions and particle properties, making it a good candidate to explain the discrepancies between theoretical predictions. Generally, a likely Dark Matter candidate would be massive, non-baryonic, and electrically neutral, and need to interact, at most, only very feebly with photons. Also, if the particle is not stable, its average lifetime must be significantly larger than the age of the Universe and that the degree of self-interaction is strongly constrained. Out of all Standard Model particles only neutrinos match this description, but due to their low mass they were relativistic in the early universe (so-called Hot Dark Matter) which would have suppressed the structure formation to an extent not seen in observations today [21]. Thus, we are left with physics beyond the Standard Model to explain the phenomenon of Dark Matter. There is a plethora of possible dark matter models and a detailed overview of the different approaches would be far beyond the scope of this thesis. Possibilities include to either have a feebly interacting massive particle such as the neutralino from some supersymmetric models or an axion-like particle as a result of trying to solve the strong CP problem. However, the search for Dark Matter particles is a difficult one, as we are largely guided by upper bounds and not precise measurements, for example on parameters such as charge or mass. Only the relative amount of Dark Matter, also referred to as the relic density, is measured precisely.

1.3 Dark Sectors

So far, there has been no compelling experimental evidence for any of the aforementioned Dark Matter candidates, but we can vastly expand our search by extending our theory. There is no a priori reason why Dark Matter should be a single particle. In principle there could be a huge number of particles that exist in this

universe but do not interact with the Standard Model particles familiar to us – a so called Dark Sector (also called Hidden Sector). This sector of particles is neutral with respect to all SM gauge groups, but could interact with each other via new, so far undiscovered forces from hidden gauge groups.

Naturally, a Dark Sector that does not interact at all is not particularly interesting to us as it would remain forever outside our grasp, but if there is some minimal interaction with the Standard Model, we can make predictions of the kind of experimental signatures a given model should provide. Additionally, some interaction is required to maintain kinetic and chemical equilibrium between the Dark Matter particles and the thermal bath of SM particles, which is a fundamental assumption required to reproduce the correct relic density through thermal freeze-out. Note that other mechanisms that set the relic density are possible, but those models differ significantly from the class of Dark Sectors presented here.

There are many possible ways a Dark Sector can couple to the Standard Model — e.g. portals through the Higgs Boson, axions or sterile neutrinos are all viable — but in this thesis the focus is on a model with a dark photon mediator as it provides arguably the most promising experimental signatures while keeping the model relatively simple. Here, dark photon refers to the force carrier of a new (dark) $U(1)$ gauge interaction which provides coupling to the SM through kinetic mixing.

Not only does a Dark Sector model have considerable freedom in the choice mediator, the structure of the Dark Sector itself can also be quite varied. In order to have a starting point rooted in familiar physics, it is helpful to start with an analogue to the Standard Model, in this case to QCD. Such a model contains dark quarks that, just like their SM counterparts, do not exist as free particles but instead form bound states, i.e. dark mesons and dark baryons, which are the Dark Matter candidates. This has the advantage of providing a good explanation why Dark Matter particles are neutral to all SM interactions as confinement often naturally leads to color, weak, and charge-neutral dark hadrons. Furthermore, a strongly interacting Dark Sector would naturally have large self interactions which helps it match the structure formation constraints from astrophysical observations. Lastly, a strongly interacting sector often exhibits a dark flavor symmetry which ensures the stability of at least some of the bound states.

1.4 Search Strategies

The search strategy presented in this thesis depends not only on the model parameters, but also on the accelerator designed to produce the possible DM candidates. High Energy experiments such as the Large Hadron Collider (LHC) largely employ missing energy searches, i.e. measuring the missing transverse energy that recoiled against visible particles. Alternatively, resonant searches that do not require the DM particle to be produced directly can be used. In both of those cases the particles of interest are either entirely stable or decay promptly. Yet many Dark Sector models predict particles with average $c\tau$ on the order of millimetres to metres, which allows us to search for a displaced vertex some distance away from the point of production. If the long-lived particle (LLP) decays into a pair of charged leptons or light charged mesons then the invariant mass of the two tracks can be used to reconstruct the LLP mass exactly, which would provide excellent sensitivity for a search. This makes displaced vertex searches with lower center of mass energies very complimentary to high energy experiments like those at the LHC which, due to necessary background suppression, have no sensitivity to LLPs with masses below ~ 10 GeV. Ultimately, this means that a QCD-like Dark Sector with a heavy dark photon mediator is a well-motivated model with a wide parameter space that provides unique signatures and is ideal for an investigation at a modern e^+e^- collider experiment such as Belle II.

Chapter 2

Belle II Experiment

Belle and BaBar were two ground-breaking B-factory experiments that were instrumental for discovering CP-violating effects in the neutral B meson system and providing experimental evidence for the Kobayashi–Maskawa hypothesis — the idea that a single complex phase could explain the CP violation in the weak interaction. This discovery was recognized by the 2008 Nobel Prize in Physics. The focus has shifted to include more physics beyond the Standard Model. As statistical uncertainties limited both Belle’s and BaBar’s sensitivity, this new focus required a B-factory with higher luminosity to create a significantly larger data sample. Subsequently, considerable upgrades have resulted in the Belle II detector, located at the similarly improved SuperKEKb electron-positron collider in Tsukuba, Japan.

2.1 Improvements over Belle

Belle II has the target of a 40-fold increase in instantaneous luminosity over Belle, which required not only considerable upgrades to both the detector and the accelerator, but the accompanying increase in backgrounds also demanded strategies to reduce resulting effects such as high occupancy levels, fake hits and radiation damage. The overall dimensions of the detector remained largely the same, as it is housed within the same 1.5 Tesla solenoid magnet and iron return yoke as the previous Belle experiment. Additionally, the expensive CsI(Tl) crystals that make up the bulk of the Electromagnetic Calorimeter could be reused and their performance

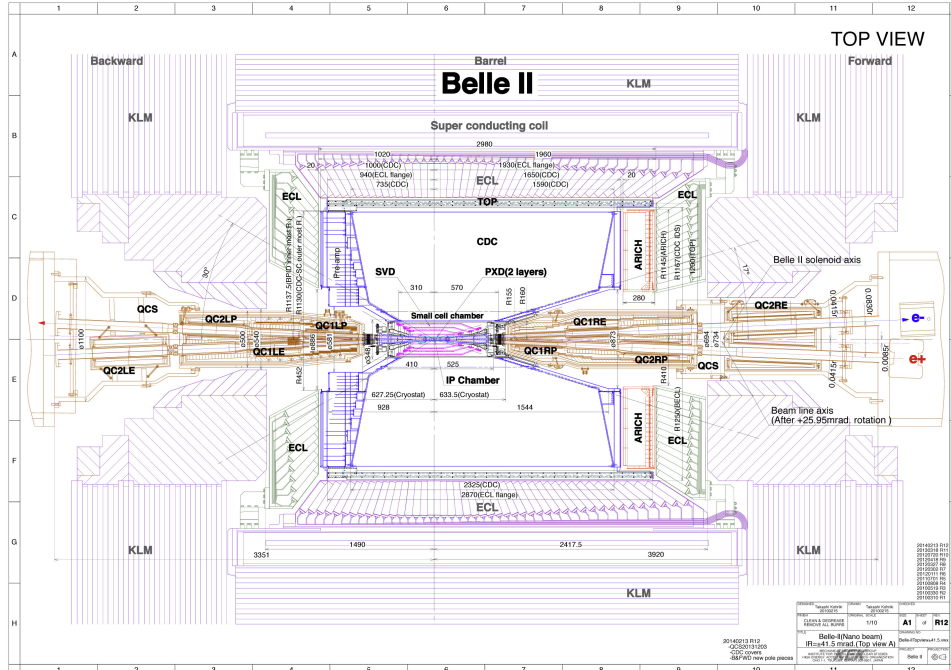


Figure 2.1: Schematic of the full Belle II Detector [18].

improved with upgraded readout electronics. The overall detector layout is shown in Figure 2.1.

2.2 Beams

As the name B-factory implies, Belle II is designed to produce and study a large number of $B\bar{B}$ pairs. To produce the desired particles in high numbers the collider runs at a center of mass energy of 10.58 GeV, corresponding to the invariant mass of the $Y(4S)$ resonance (which corresponds to colliding a 7 GeV electron and a 4 GeV positron in the laboratory frame). This resonance is a bound state of a b quark and a b antiquark that is of particular interest as it is the first epsilon meson state whose mass is high enough to allow it to decay into a B mesons pair. Since the difference in mass between a $Y(4S)$ and 2 B mesons is approximately $20 \text{ MeV}/c^2$, the two B are produced almost at rest in the center-of-mass (CM) frame. Due to the short lifetime of B mesons ($\tau_{B^\pm} = 1.638 \times 10^{-12} \text{ s}$, $\tau_{B^0} = 1.519 \times 10^{-12} \text{ s}$), the relative

displacement between the production and decay vertices is of the order of $60 \mu\text{m}$ at SuperKEKb, which has motivated the design choice of asymmetric beam energies. This ensures that the collision products experience a considerable Lorentz boost ($\beta\gamma = 0.28$), making the measurement of the particles' proper time significantly easier.

B mesons can be produced in e^+e^- or in hadronic interactions. The production in hadronic interactions at high energy (for instance in $p\bar{p}$ collisions at 13 TeV at LHC) offers a large cross-section and a large spectrum of possible collision products, but electron-positron colliders have the advantage of producing cleaner events. This is especially advantageous for investigating rare decays as it allows for simpler triggering and event selection.

2.3 Interaction Point

To facilitate the desired increase in luminosity a variety of improvements were made to the accelerator. A large improvement is due to the 'nano-beam scheme' which reduced the size of the beams at the Interaction Point (IP) ¹. Additionally, the beam currents were increased by a factor of 2 and the beam emittance was minimized through a combination of reducing the difference in beam energies, adjusting the length of the dipole magnets and installing wiggler magnets. These changes naturally lead to higher beam background rates. In the rest of this chapter r refers to the radial distance, i.e. $\sqrt{x^2 + y^2}$, from the IP while z refers to the distance along the cylindrical axis of the detector.

2.4 Pixel Detector

The Belle II Vertex Detector (VXD) consists of two layers of Pixel Detector (PXD) at a distance from the IP of $r = 14 \text{ mm}$ and $r = 22 \text{ mm}$, followed by 4 layers of silicon strip detectors (called SVD).

¹Specifically it reduces the vertical beta function of the beam by a factor of 20 compared to the previous experiment with a smaller but still significant improvement in the horizontal beta function. This however worsens the so-called "hour-glass effect", which lowers the effective luminosity due to the variation of the transverse beam size along the length of each bunch. It occurs if the beam is small compared to the bunch length but is compensated for by increasing the crossing angle to 83 mrad, which allows the final focusing magnets to be much closer to the IP

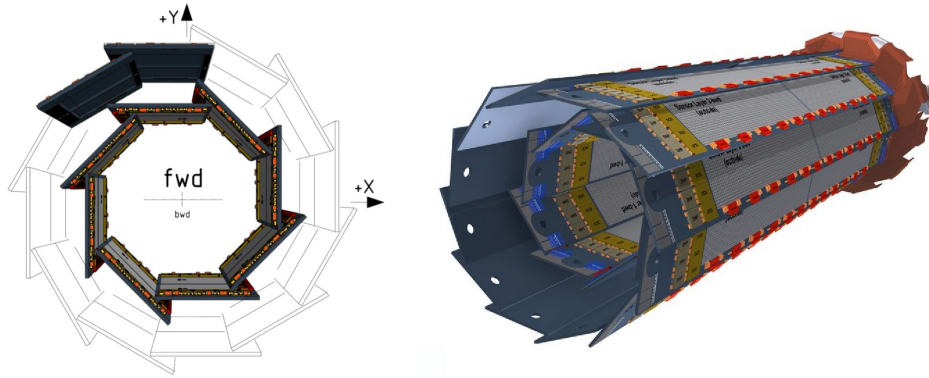


Figure 2.2: Left: Shows the number and position of currently installed PXD sensors. Right: Shows the full PXD design to be implemented in 2023 [27].

Pixel sensors have a much larger number of channels compared to strip sensors and therefore a much smaller occupancy and were previously implemented at the LHC with great success. The LHC pixel sensors however are much too thick and would cause too much scattering for a precise reconstruction of B-decay vertices at Belle II energies. Instead, sensors based on DEPFET (DEPLETED Field Effect Transistor) technology were chosen which allows for very thin (50 micron) sensors due to their internal amplification.

A single DEPFET pixel cell consists of a p-channel field effect transistor (FET) which is placed on fully depleted n-doped silicon bulk material and so combines the functions of a charge collecting electrode and a FET. A phosphorus implantation shifts the potential minimum formed by sideways depletion underneath the transistor channel which forms what is called an internal gate that modulates the current through the MOSFET on the readout.

The most important feature of the DEPFET is the very small capacitance of the internal gate, resulting in a very low noise performance even at room temperature. Additionally the gate is on only during readout, which leads to a very low power consumption that allows for the use of gas injection cooling to cool the sensors themselves. Meanwhile the readout electronics, which need active cooling, are located outside the acceptance region, and therefore do not add additional material

in the detector volume.

The DEPFET pixels are assembled into 250×768 pixel modules and surrounded by a silicon frame to form self-supporting structures. The modules contain smaller pixels ($50 \times 55 \mu\text{m}$) on the end closer to the IP and slightly larger ($50 \times 70 \mu\text{m}$) at the end further from the IP. Two mirrored modules are glued end to end lengthwise to form a ladder. The complete detector consists of two cylindrical layers, 8 ladders at a distance of 14mm and 12 ladders at 22mm from the interaction point, for a total of about 8 million pixels. The sensitive part of the modules is thinned down to a thickness of $75 \mu\text{m}$ ($50 \mu\text{m}$ for the pixel sensor and $25 \mu\text{m}$ for the supporting structure). This and the self supporting design result in each layer only being about 0.2% radiation lengths per layer. Due to difficulties in the manufacturing process and subsequent delays only the full inner layer and two ladders of the outer layer were ready for initial installation in 2019, as shown in Figure 2.2, with the rest of the detector being installed during the 2022-2023 shutdown.

2.5 Silicon Strip Detector

The Silicon Vertex Detector (SVD) is made of Double-Sided Silicon micro-strip Detectors, at radii of 39 mm, 80 mm, 104 mm, and 135 mm, arranged in such a way that the large pitch strips are perpendicular to the beam direction while small pitch side strips are parallel to the beam. This provides both x and y coordinates of the hits. The innermost SVD layer has small rectangular sensors while the other three layers are composed of two types of sensors: large rectangular sensors for the barrel region and slanted sensors with a trapezoidal shape which reduces the material budget and improves acceptance and precision for forward boosted particles. The layout and sensor dimensions are shown in Figure 2.3.

The so-called “Origami” chip-on-sensor design concept was developed for the Belle II SVD, which has thinned the readout application-specific integrated circuits (ASICs) in the active volume of the detector. The average material budget for one ladder including ribs, silicon strips, electronics and cooling pipes is about 0.7% of a radiation length.

Strip sensors are used not only to save cost, but it also to make up for some of the other drawbacks of pixel detectors; the PXD provides better spatial resolution

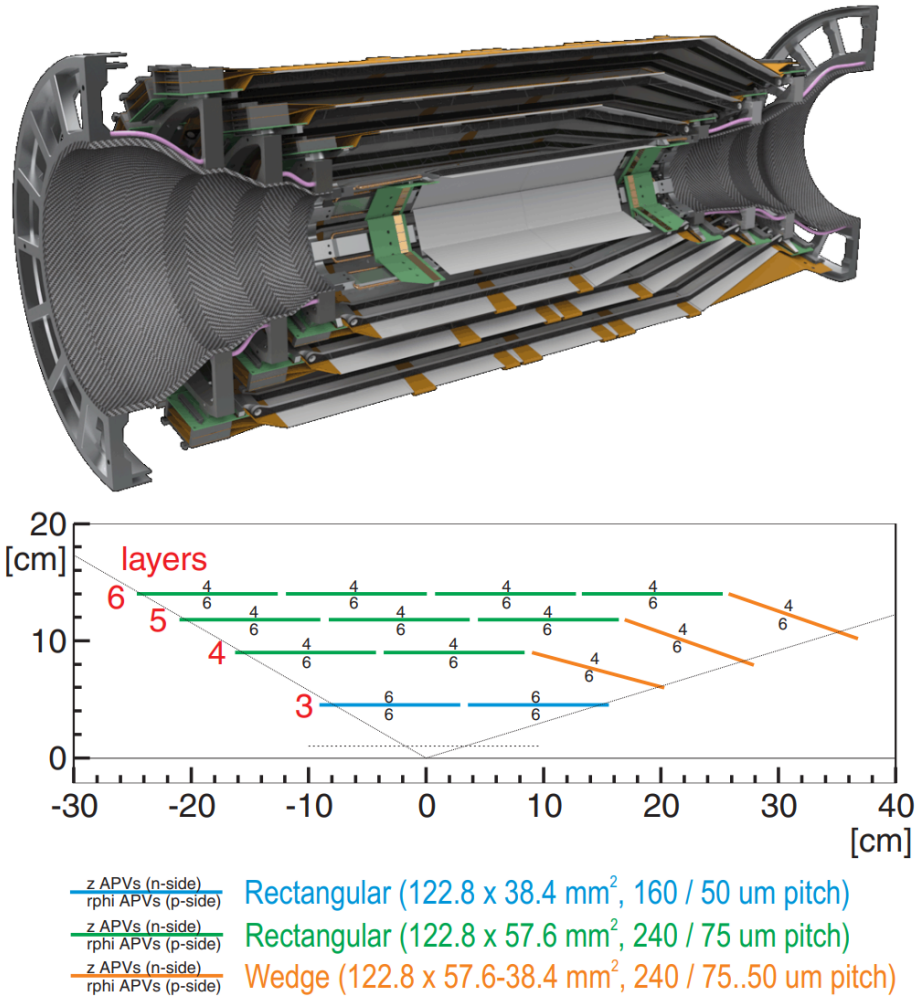


Figure 2.3: Top: A graphic display of the SVD surrounding the PXD. Bottom: The position and dimensions of the different SVD sensors [10].

but is quite slow due to a long integration time while the SVD provides better timing resolution. This strip detector extends further than its predecessor as the background level at radii as large as ~ 10 cm were estimated to be too high to use a conventional drift chamber. This also allows the SVD to reconstruct the decay vertices of neutral particles such as K_s^0 mesons.

2.6 Drift Chamber

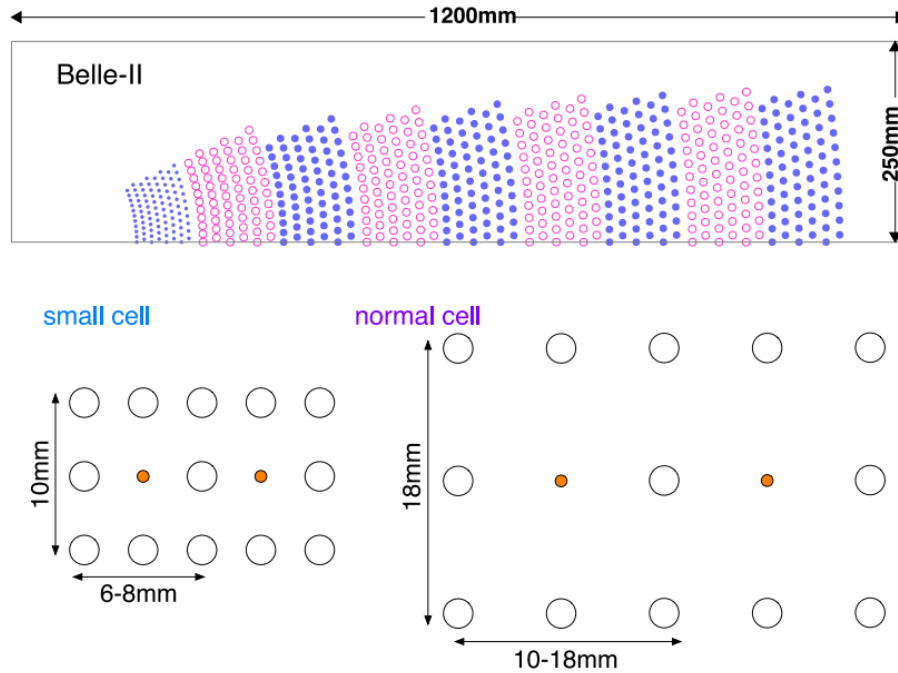


Figure 2.4: Top: Wire configuration for the Belle II CDC. Blue and pink represent axial and stereo (anode) wires respectively. Bottom: CDC cell dimensions for small and large cells. Large white and small orange circles denote the cathode and anode wire respectively [1].

The Belle II (Central Drift Chamber (CDC)) is a large volume gas drift chamber that, similarly to the SVD, uses similar design choices as Belle in terms of material and layout but with upgraded electronics. It fulfills a variety of tasks, the most straightforward one being the reconstruction of tracks of charged particles and measurements of their momenta. It is also used for particle identification, using the fact that different particles have different energy loss profiles, which is especially important for low-momentum tracks that do not reach the designated particle identification subcomponents. Lastly, it provides the majority of signals for the trigger system for charged particles.

The overall design was retained from Belle and can be described in terms of

cells and superlayers, as illustrated in Figure 2.4. Each cell is a 3 by 3 cluster of wires, i.e. an anode wire surrounded by 8 cathode wires in square configuration, with side length of 18 mm. The exception is the innermost layer which has a smaller cell size of 10 mm to reduce the occupancy in the face of the large beam background. To match the requirement of the readout electronics there are 32 cells per layer. A 'superlayer' is formed by 6 layers of (anode) wires, again with the exception of the innermost one which contains two additional active guard wires. In total there are nine superlayers in so-called AUV ordering, where A stands for Axial, U for positive stereo angle and V for negative stereo angle. While the axial wires are oriented in parallel to the beamline, the stereo wires are skewed to allow for 3D reconstruction of the tracks. A 50/50 gas mixture of helium and ethane is used as in Belle.

As described earlier, the inner radius of the CDC is much larger compared to Belle as the hit rate at 100 mm would be too high for a drift chamber, with the area instead covered by the SVD. In turn, the CDC extends to a larger outer radius, specifically from 160 mm to 1130 mm.

2.7 Particle Identification

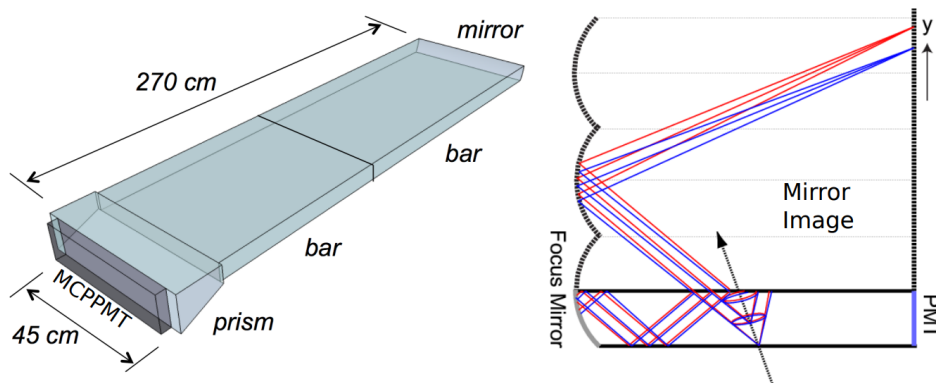


Figure 2.5: Left: Shows the overall design of the TOP counter. Right: Shows the operating principle and purpose of the focusing mirror, ensuring that parallel rays are focused to the same point on the sensor [24].

Belle II uses two main subcomponents for particle identification, a Time of

Propagation (TOP) counter in the barrel region and an Aerogel Ring Imaging Cherenkov (ARICH) in the forward facing endcap.

The TOP consists primarily of 16 large quartz bars that surround the outer wall of the CDC. In the quartz crystals a passing charged particle emits Cherenkov photons in a cone with an opening angle determined by the particle velocity. Thus, assuming that the momentum is precisely measured by the inner subdetectors (CDC in particular), the characteristic Cherenkov cone will be unique for particles of different mass and can be used to identify the particle. The Cherenkov photons are transported to the end of the quartz bar via total internal reflection where they are detected using micro-channel plate photomultiplier tubes (MCP PMTs). This allows for a 3D reconstruction of the Cherenkov cone (in x , y position and time). Between the bar and the readout electronics there is a small expansion volume (about 10 cm long) to slightly lower the precision timing requirements and reduce the hit occupancy at the photo-detector. Since the resolution is primarily limited by chromatic dispersion, a spherical mirror is added to the end of the quartz bar which allows photons with different wavelengths (and thus Cherenkov angle) to focus into different areas of the MCP. The design and operating principle is shown in Figure 2.5.

The ARICH particle identification system consists primarily of an aerogel radiator, where Cherenkov photons are produced by charged particles, and an array of photon detectors that are capable of detecting single photons with high efficiency and good 2D resolution. Between the aerogel and the photon detectors there needs to be an expansion volume to allow Cherenkov photons to form distinct rings. The requirements of creating enough detectable photons and the limit of the resolution of the photon detectors give a radiator thickness of about 2 cm followed by an approximately 20 cm gap.

2.8 Electromagnetic Calorimeter

The primary task of the Electromagnetic Calorimeter (ECL) is to detect and measure the energy of photons over a wide range of energies but also to identify electrons and distinguish them from pions. It is split into three regions, the barrel, forward endcap and backward endcap, which covers 90% of the solid angle of the

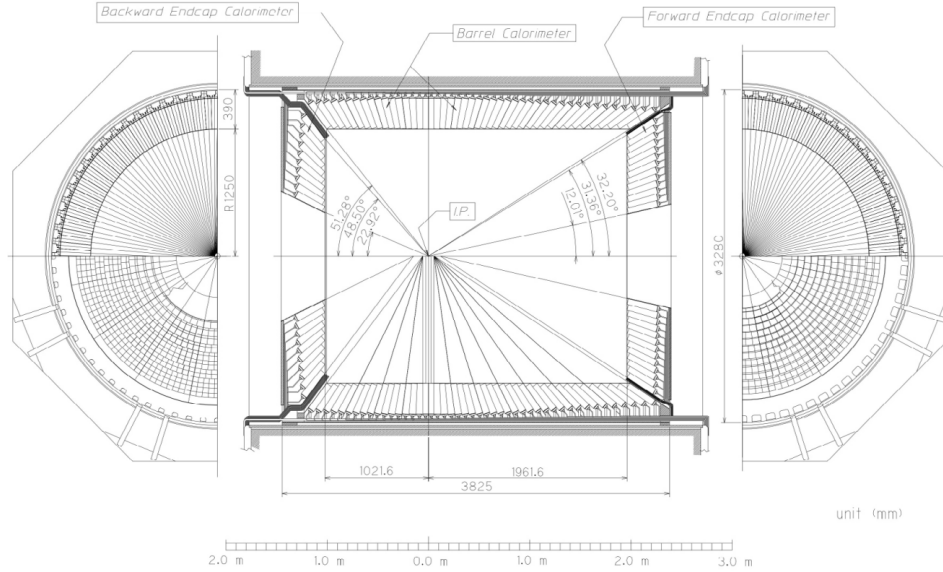


Figure 2.6: Schematic of the Belle II ECL and detailed crystal layout [1].

detector. The ECL consists of 8736 thallium-doped cesium iodide CsI(Tl) crystals, each $60 \text{ mm} \times 60 \text{ mm}$ in cross section and 300 mm in length which corresponds to about 16 radiation lengths. The crystal layout can be seen in Figure 2.6.

Each crystal is wrapped with a layer of porous teflon and covered by a laminated sheet of $25 \mu\text{m}$ thick aluminum and $25 \mu\text{m}$ thick mylar. For scintillation light readout, two $10 \times 20 \text{ mm}$ photodiodes are glued to the rear surface of the crystal on top of a 1 mm thick acrylic plate. This allows for two independent outputs to be summed in the readout electronics. The crystals are inherited from the previous Belle experiment but with the increased background levels at Belle II the relatively long decay time of CsI(Tl) crystals ($\sim 1 \mu\text{s}$) causes a considerably increase in the overlapping of pulses from close events. To better separate these, the readout electronics were upgraded to not only be faster but also to include waveform sampling.

2.9 K_{long} and Muon Detector

The K_{long} and Muon Detector (KLM) is the outermost subdetector and is, similar to the ECL, split into 3 regions. It is a series of 4.7 cm thick layers of iron alternating

with active scintillating material, where the iron not only provides material for the muons and kaons to shower hadronically, but also acts as a magnetic flux return for the solenoid. The bulk of the subdetector operates based on glass-electrode Resistive Plate Chambers (RPC's) but due to the long dead time of RPCs and the increased hit rate over Belle, both endcaps and two innermost layers of the barrel region instead use scintillator strips with wavelength-shifting fibers. A summary of subdetector components and dimensions is given in Table ??.

2.10 Software

The Belle II Analysis Software Framework (BASF2) is the primary software used for most aspects of data processing at Belle II, including but not limited to generating simulated data, unpacking of raw data, reconstruction (tracking, clustering, etc.), and higher level analysis such as applying cuts and vertex fitting [19].

The code is written in C++, partitioned into about 40 packages such as the base-level framework, with one package for each detector component, the track reconstruction code, and the post-reconstruction analysis tools. The execution of these modules is handled by script files written in python.

Basf2 can also interface with third-party software that is bundled in the externals installation, most importantly ROOT, as root files are the primary form of data storage in the context of basf2 analysis, and GEANT4 [3], which simulates the detector interaction during MC generation .

2.11 Trigger

The trigger system at Belle II is of vital importance to selecting events of interest while rejecting the large background that primarily stems from intra-beam and Bhabha scattering. The displaced vertex signatures discussed in this thesis are especially difficult to trigger due to the small number of final state particles in them. The following chapter briefly summarized the triggering strategies at Belle II and outlines future improvements relevant to this analysis. Belle II employs both a hardware (called Level 1 or L1) and a software trigger (called the higher level trigger or HLT).

2.11.1 Level 1 Trigger

The L1 trigger system consists of sub-trigger systems for each subdetector and one final decision logic called the Global Decision Logic (GDL). Each sub-trigger system summarizes trigger information through a partial event reconstruction before sending it to the GDL where it is checked whether or not a particular combination of sub-triggers satisfies a given triggering criteria. The event is only fully read out on a successful L1 Trigger.

The requirements for the L1 trigger system are:

1. Close to 100% efficiency for hadronic events from $\Upsilon(4S) \rightarrow B\bar{B}$ and $e^+e^- \rightarrow q\bar{q}$
2. High efficiency for low multiplicity physics
3. A maximum average trigger rate of 30 kHz
4. Fixed latency of about 5 μs
5. Timing precision of less than 10 ns
6. Minimum two-event separation of 200 ns

and in general a design that allows the trigger configuration to be both flexible and robust.

To facilitate this, each component has a Field Programmable Gate Array (FPGA) which allows for some configuration, rather than being hard-wired. This is especially important as it allows the implementation of a neural network to reconstruct the z (longitudinal) position of the event vertex, allowing the suppression of events not originating at the IP. Each subdetector has a distinct contribution to the overall trigger system. The CDC sub-trigger provides the charged track information such as momentum, position, and charge and thus provides the most important components to the L1 trigger. It also defines the latency of the L1 trigger due to the long drift times of the wire signals. The ECL sub-trigger gives energy deposit information, energy cluster information, Bhabha identification, and cosmic-ray identification. The TOP sub-trigger gives precise timing and hit topology information. The

KLM sub-trigger gives muon track information. The Global Decision Logic receives all of this sub-trigger information and makes the final decision of accepting or rejecting the event. Notably the L1 trigger does not use any information from the PXD or SVD as the readout is too slow to provide information at the required rate [15].

The track trigger processes four different modules in its pipeline. The Track Segment Finder first minimizes the amount of data sent to the next module by combing the raw CDC hits in a given superlayer into a short track segment, which also suppresses noise from isolated hits. The 2D Finder then combines track segments from the axial superlayers to full tracks in the x - y plane using a Hough transformation. At the same time, the Event Time Finder module determines the event time for precise spatial information from the hits. Normally, event timing would be provided by the TOP or ECL, but due to the pipelined nature of the trigger system this information is not available, so all timing information for tracks at the L1 trigger level have to come from the CDC. Finally the last module, called Neurotrigger, uses the 2D track information and related stereo hits to estimate a z -vertex position and polar angle θ for the track. To do so, it uses artificial neural networks onto the FPGA hardware which allows for very fast processing and also provides the ability to learn non-linear correlations in data. The Neurotrigger is of essential importance as it is the primary tool to reject background events with a low track count [16]. For events with few particles in the final state, the most important trigger requires the presence of one reconstructed 3D track (also called a Neuro track).

2.11.2 Higher Level Trigger

While the L1 trigger is very successful at filtering out background events the data flow still needs a significant subsequent reduction to a manageable level. This is done via the high level trigger (HLT) which uses full offline event reconstruction to perform physics-level event selection [20]. Notably there are two data streams: one from the PXD and one from the other subdetectors. The PXD system takes at least $20 \mu s$ to read out the entire detector and therefore there is a high probability that the next trigger arrives before completing a single readout cycle. For all subdetectors

except the PXD, the L1 trigger signal is distributed to the detector front-end and initiates the data transfer from the subdetectors. The signals are digitized at the detector front-end and transferred to common readout cards (called COPPER's). On each card a Linux-operated CPU performs the data formatting and reduction before the data is sent to readout PCs. There the event fragments are collected and formatted into one (partial) event for each subsystem before being sent to the HLT units. For the PXD readout, the tracks of charged particles reconstructed by the HLT with information from the SVD and CDC are extrapolated to the surface of PXD sensors where it creates regions of interest. Then, only hits from regions of interest are read out reduces the data transmitted by the PXD by a factor of 10 compared to a full readout. Under the nominal accelerator condition, the overall reduction factor by the HLT trigger is measured to be about 8, which is more than the design value, because of the high background conditions [14].

Chapter 3

Theory

As motivated in Chapter 1, the model that will be investigated in this thesis is that of a strongly interacting dark sector with a dark photon mediator that results in a displaced vertex signature as illustrated by Figure 3.1. This chapter provides a brief summary of the model and key aspects of its derivation, for a full derivation see reference [7].

3.1 Lagrangian construction

To construct the model we start by considering a number N_f of fermions with some underlying gauge group. We refer to the fermions as dark quarks and to the gauge bosons of the new sector as dark gluons. While the underlying gauge group could theoretically be any group that leads to confinement for N_f dark quarks, the focus is on a $SU(3)$ gauge group in analogy to classical QCD. Additionally, it should be pointed out that just like for classical QCD the strong coupling of the dark sector diverges at the energy scale Λ_d . Close to the scale Λ_d the coupling becomes non-perturbative, making it impossible to calculate predictions for hadronic interactions at low energies. In order to have an model formulation that is valid at energies $E \sim \Lambda_d$ the corresponding Lagrangian is phrased as a chiral Effective Field Theory (EFT) and reads as follows:

$$\mathcal{L}_d = -\frac{1}{4}G_{d\mu\nu}^a G_d^{\mu\nu,a} + \bar{q}_{di} i\not{D}q_{di} + \bar{q}_{di} (M_{q_d})_{ij} q_{dj}$$

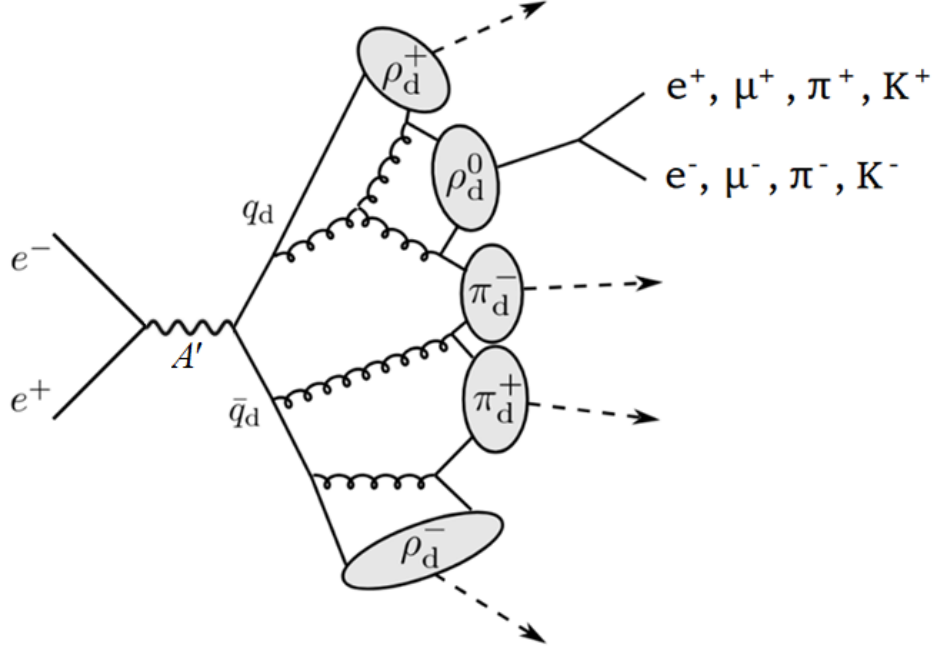


Figure 3.1: Illustration of a Dark Shower Event with one ρ_d^0 meson.

where $G_{d\mu\nu}^a$ denotes the dark gluon field strength, q_d denotes the dark quarks, $i = 1 \dots N_f$ is the dark quark flavour index, and M_{q_d} is the dark quark mass matrix. The running of the dark coupling constant:

$$\alpha_d(\mu^2) = \frac{1}{\frac{1}{4\pi}(11 - \frac{2}{3}N_f)\ln(\frac{\mu^2}{\Lambda_d^2})}$$

leads to confinement at the scale Λ_d . Below this scale the dark quarks form bound states, i.e. dark mesons and baryons, in particular $N_f - 1$ pseudoscalar dark pions and vector meson dark rhos. In theory, even restricting to a QCD-like dark sector with a given mediator, we still have considerable freedom when it comes to the choice of what actually constitutes the dark matter. While dark baryons or dark glueballs can both make viable candidates, we will focus on the case of dark mesons by choosing the dark quark mass much lower than the confinement scale. Thus, the dark matter for this model consists of the dark pions mentioned above

and can be described by a chiral EFT, in complete analogy to the description of light QCD mesons. All three dark sector pions, π_d^+ , π_d^- , and π_d^0 , are stable and equally contribute to the dark matter abundance. The neutral dark vector meson ρ_d^0 is of particular importance as it provides the portal to the standard model. Analogous to the mixing of the standard model rho with the photon, the ρ_d^0 mixes with the A' which introduces a small coupling to the SM, making the ρ_d^0 unstable and ultimately resulting in our desired displaced vertex signature.

For the sake of simplicity, we will consider a model where the dark sector only has 2 flavors, as opposed to the 6 in classical QCD. This is to consider a minimal scenario that is cosmologically viable and can account for DM in the form of dark pions while ensuring that the lightest neutral dark pion is completely stable.

Naturally we also need to include the mediator itself in our model. The theoretical framework for this and many other dark photon models is created by introducing a new $U(1)'$ gauge symmetry under which both dark and SM quarks are charged. The dark photon is the associated gauge boson of this new symmetry and can mix with the $U(1)_Y$ gauge boson of the SM (i.e. the B boson of the weak hypercharge) and thus mediates interactions between the SM and the dark sector. We have two interactions of the form:

$$\mathcal{L}_{SM-int} \supset -g_q A'_\mu \sum_{q_{SM}} \overline{q_{SM}} \gamma^\mu q_{SM}$$

where g_q denotes the quark- A' coupling, i.e. the product of the $U(1)'$ gauge coupling and the quark charges. In the dark sector we combine the $U(1)'$ charge assignments of the dark quarks into a charge matrix Q , such that the A' interaction in the unconfined dark quark takes the form:

$$\mathcal{L}_{d-int} \supset -e_d A'_\mu \overline{q_{SM}} \gamma^\mu Q q_d$$

where we have introduced the coupling e_d , which is the product of the $U(1)'$ gauge coupling and the dark quark charge.

Furthermore it is assumed that the A' obtains a mass $m_{A'}$ through the Stückelberg mechanism, a special case of the Higgs mechanism. One can diagonalize the ki-

netic terms by redefining the fields to eventually obtain the Lagrangian:

$$\mathcal{L} = -\frac{1}{4}F'_{\mu\nu}F'^{\mu\nu} + \frac{1}{2}m_{A'}^2 A'^2 - \kappa e A'_\mu \sum_f q_f \bar{f} \gamma^\mu f - e_d \bar{q}_d \gamma^\mu q_d$$

where κ is the kinetic mixing parameter and e_d is the dark sector coupling strength. Since lower dark photon masses are well covered by other experiments we are interested only in off-shell dark photons, i.e. those with a $m > 10.58 \text{ GeV}/c^2$. This lets us integrate out the mediator in the Lagrangian above to obtain an effective interaction between SM fermions and dark quarks given by:

$$\mathcal{L}_{eff} \supset \frac{1}{\Lambda^2} \sum_f q_f \bar{f} \gamma^\mu f \bar{q}_d \gamma_\mu q_d = \frac{2}{g} \frac{m_{\rho_d}^2}{\Lambda^2} \rho_d^{0\mu} \sum_f q_f \bar{f} \gamma_\mu f$$

Where g is the dark pion-rho coupling strength which is set to 1. The scale Λ determines the strength of the interaction and is given by

$$\Lambda = \frac{m_{A'}}{\sqrt{\kappa e e_d}}$$

This has the great advantage that the off-shell production of dark quarks depends only on the mediator's properties through the effective coupling Λ , which allows us to drop $m_{A'}$, κ , and e_d and discuss the phenomenology only in terms of the effective interaction. Instead of discussing the phenomenology in terms of Λ , we can simply present it as only depending on the mass of the ρ_d^0 and its lifetime.

3.2 Relic Density

In the early Universe the decays and inverse decays of the ρ_d^0 can keep it in equilibrium with the thermal bath of SM particles. Strong interactions between ρ_d^\pm and ρ_d^0 keep the charged dark rho mesons in equilibrium with the neutral dark rho mesons and thus, in turn, with the SM bath. The same holds for our DM candidates, the dark pions, which maintain equilibrium with the ρ_d^0 , and thus the SM, through strong $\pi_d - \rho_d$ interactions. In this way, the entire dark sector is initially in equilibrium with the SM and DM freeze-out occurs when $\pi_d - \rho_d$ conversions become inefficient. Therefore, the dominant process we need to consider is the

(forbidden) annihilation of $\pi_d\pi_d \rightarrow \rho_d\rho_d$. This mechanism allows us to obtain the correct DM relic density over many orders of magnitude in the DM mass as long as the ratio m_{ρ_d}/m_{π_d} is adjusted accordingly, though it makes the generic prediction that the mass difference between dark pions and dark rho mesons has to be small. For the purpose of phenomenological studies in this thesis, the dark pion mass was kept roughly equal to the dark rho mass as small fluctuations in the dark pion mass had no significant impact on experimental signatures.

3.3 Parameter Space

While it is very convenient to parametrise the mediator properties of the ρ_d^0 only through its mass and lifetime, it is still necessary to ensure that the combination corresponds to a value of Λ_d with viable coupling strengths. At minimum, it is required that the kinetic mixing parameter fulfills the mass-independent upper bound $\kappa < 0.026$ and that the dark sector coupling is perturbative, i.e. $e_d < \sqrt{4\pi}$.

Additionally, we have bounds on the DM self-interaction cross section from astrophysical observations which puts a lower bound of $100 \text{ MeV}/c^2$ on the mass of the ρ_d^0 . In order for the confinement scale to lie sufficiently far below the CM energy of Belle II we have an upper bound on the ρ_d^0 mass of approximately $2 \text{ GeV}/c^2$. These bounds are shown in Figure 3.2.

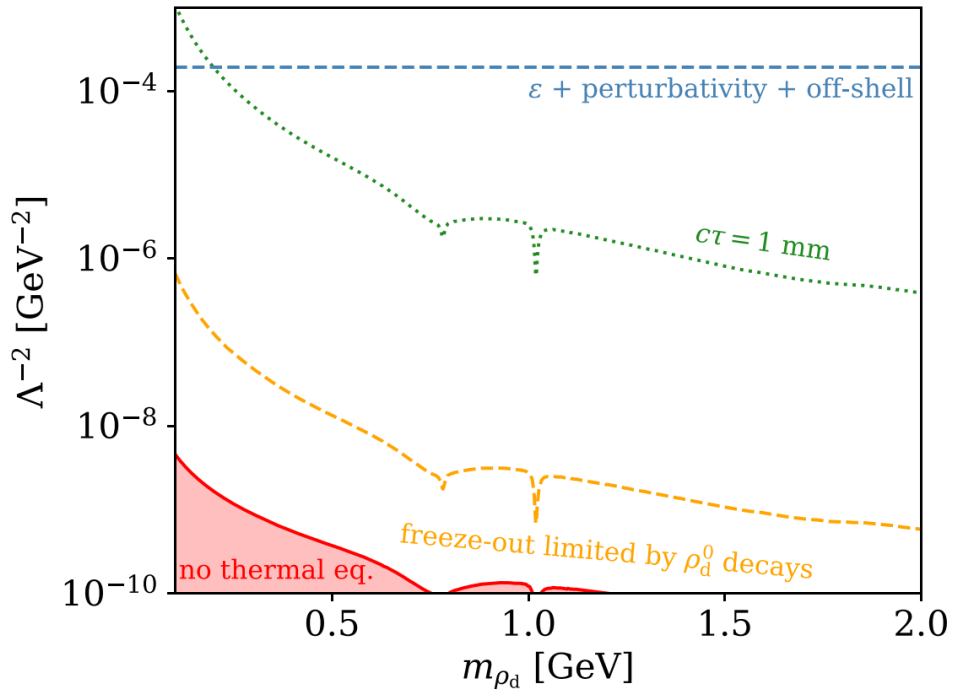


Figure 3.2: Below the red line, dark rho and pions are not in thermal equilibrium, which is required to obtain the correct relic density during freeze-out. The blue dashed line represents a mass-independent consistency bound on Λ . The area below the green dotted line indicates where dark rhos are expected to be sufficiently displaced [7].

Chapter 4

Analysis Structure and Event Selection

The key signature of our long-lived particle is one or more displaced vertices, with a variety of possible final state particles. The ρ_d^0 can decay to a pair of leptons, i.e. e^+e^- or $\mu^+\mu^-$, or it can decay hadronically to pions and/or kaons. The relatively unique nature of a displaced vertex signature allows for the possibility of a zero-background analysis, the feasibility of which is explored in this thesis.

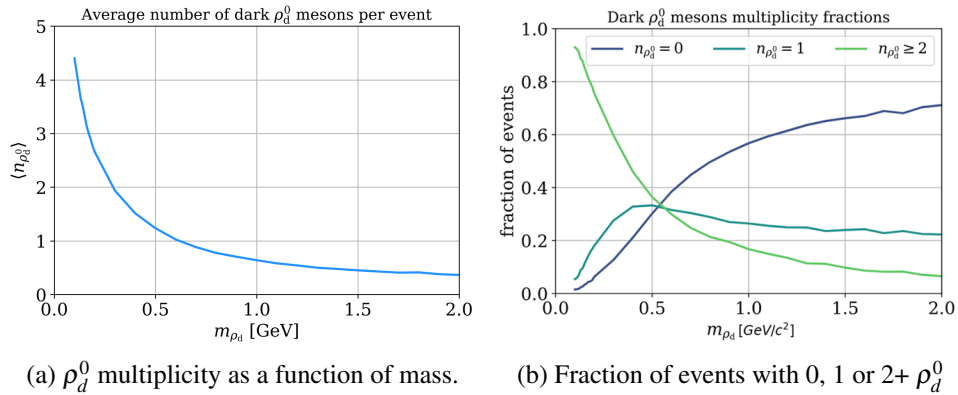


Figure 4.1: For a mass below $500 \text{ MeV}/c^2$, the majority of events contain multiple ρ_d^0 and therefore multiple displaced vertices. For larger masses a significant fraction of events contain no ρ_d^0 and so require a different search strategy like single-photon searches [7].

The average ρ_d^0 multiplicity is shown in Figure 4.1a. It decreases quickly with the dark rho mass, so that for $m_{\rho_d^0} < 500 \text{ MeV}/c^2$ the majority of events contain multiple decaying dark mesons, while for larger masses a significant fraction of events contain no ρ_d^0 .

In order to provide meaningful feasibility study without exceeding the scope of the thesis, the focus will be on events with a single displaced vertex with only muons in the final state. In this case, the invariant mass of the two tracks reconstructs the ρ_d^0 mass exactly, which should provide a very strong and clear signal peak. At the same time, the muon final state allows for an excellent reduction of background (compared to the e^+e^- case where a significant amount of photon conversions is to be expected, complicating the background reduction).

4.1 Signal Generation

For the signal event generation, the starting point is a UFO (Universal Feynrules Output) model file. This model file is a result of feeding the unconfined dark quark Lagrangian into the FEYNRULES package [4] to encode the model information into a python module. This UFO file was obtained from the author of the primary theory paper that this thesis is based on [7].

$$\mathcal{L} = -\frac{1}{4}F'_{\mu\nu}F'^{\mu\nu} + \frac{1}{2}m_{A'}^2 A'^2 - \kappa e A'_\mu \sum_f q_f \bar{f} \gamma^\mu f - e_d A'_\mu \bar{q}_d \gamma^\mu q_d$$

This UFO file is then loaded in MADGRAPH5_AMC@NLO 2.6.4 [5] to generate partonic events at leading order for the dark quark production process $e^+e^- \rightarrow q_d \bar{q}_d$. To perform the showering and hadronisation in the dark sector the Hidden Valley module of PYTHIA 8 was used [25]. All decays are simulated as prompt in PYTHIA 8 and subsequently all particles in the decay chain are displaced in basf2 by decay lengths that are randomly drawn from an exponential distribution fitting the corresponding average lifetime.

From our effective interaction Lagrangian in Chapter 3, we can obtain the partial width for the decay of ρ_d^0 to lepton pairs:

$$\Gamma(\rho_d^0 \rightarrow \ell^+ \ell^-) = \frac{1}{3\pi g^2} \frac{m_{\rho_d}^5}{\Lambda^4} \left(1 - 4 \frac{m_\ell^2}{m_{\rho_d}^2}\right)^{1/2} \left(1 + 2 \frac{m_\ell^2}{m_{\rho_d}^2}\right)$$

To find the hadronic decay width of the ρ_d^0 we can use the fact that it inherits the coupling structure of the dark photon, which has the same coupling structure as the SM photon, so its decay width can be determined by using the measured hadronic R ratio at e^+e^- colliders defined as:

$$R\left(\sqrt{s} = \frac{\sigma(e^+e^- \rightarrow \text{hadrons})}{\sigma(e^+e^- \rightarrow \mu^+\mu^-)}\right)$$

so that:

$$\Gamma(\rho_d^0 \rightarrow \text{hadrons}) = R(\sqrt{s} = m_{\rho_d})\Gamma(\rho_d^0 \rightarrow \mu^+\mu^-)$$

In practice the branching ratios were obtained using the dark shower tool developed by Knapen et. al. [17], which matches the R ratio calculations for the most common decay modes but proved to be significantly more convenient to use. The decay modes considered for this analysis are:

- $\rho_d^0 \rightarrow e^+e^-, \rho_d^0 \rightarrow \mu^+\mu^-$
- $\rho_d^0 \rightarrow \pi^+\pi^-, \rho_d^0 \rightarrow K^+K^-$
- $\rho_d^0 \rightarrow \pi^+\pi^-\pi^0$
- $\rho_d^0 \rightarrow \pi^+\pi^-\pi^+\pi^-$
- $\rho_d^0 \rightarrow \pi^+\pi^-\pi^0\pi^0$

A plot showing the relative branching ratios as a function of ρ_d^0 mass is shown in Figure 4.2.

4.2 Background

There are a variety of possible SM processes that can produce a lepton or meson pair that can mimic our desired signal signature of one (displaced) vertex with missing energy. One example is direct lepton and meson pair production, i.e. $e^+e^- \rightarrow \mu^+\mu^-$, possibly in association with one or more photons that are outside

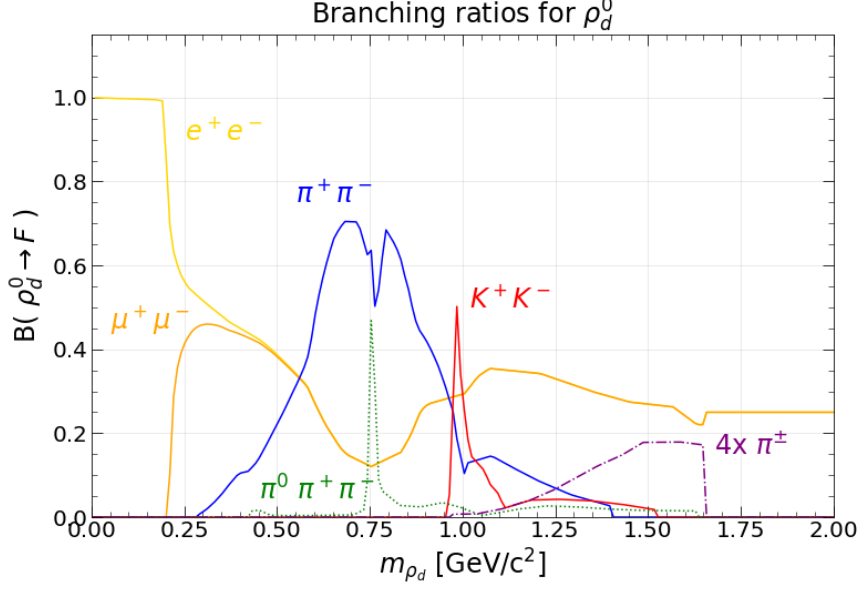


Figure 4.2: Individual branching ratios of the ρ_d^0 as a function of its mass. The coupling structure is directly inherited from the A' mediator.

of detector acceptance or not reconstructed for other reasons. Requiring a minimum displacement for the vertex location removes a large portion of the prompt SM background. Meson decays, specifically $e^+e^- \rightarrow \phi, \phi \rightarrow K_S^0 + K_L^0, K_S^0 \rightarrow \mu^+\mu^-$ are not removed by that requirement as K_S^0 have a sufficiently long lifetime to create a displaced vertex. This can be effectively dealt with by vetoing the mass region around the K_S^0 peak but this naturally has the disadvantage of losing sensitivity for detecting ρ_d^0 with similar mass. Lastly, photon conversions, i.e. $\gamma \rightarrow e^+e^-$, where the missing energy is also carried off by an undetected photon, are likely a considerable source of background for events where the dark rho decays to electrons, but is not as relevant for the muon signal discussed in this thesis.

With these considerations, most of the remaining background is due to random track overlap and material interactions. We identify the three most prominent background contributions as:

1. events with two taus which subsequently decay to muons. The random track

overlap from the muons fakes a displaced vertex and a significant amount of energy is missing due to the production of neutrinos

2. Similarly, production of a K^+K^- pair which decays to muons and a neutrino
3. Hadronic events which produce pions that end up being misidentified as muons

Requiring a displaced vertex is by itself already a strong condition to reduce background levels but further reduction can be achieved by splitting the detector into multiple sub-regions by their distance from the IP (denoted dr), three of which can be used in this analysis. The choice of regions is largely determined by the material distribution and sub-detector location as motivated by [12].

Region 0 $0 \text{ cm} \leq dr \leq 0.2 \text{ cm}$: This region is very close to the interaction point which results in prohibitively large SM backgrounds, leading to a minimum required vertex displacement of 0.2cm, meaning that this region is not included in the analysis.

Region 1 $0.2 \text{ cm} < dr \leq 0.9 \text{ cm}$: In this region the vertex is still inside the beam pipe but sufficiently far away from the interaction point that prompt SM backgrounds are fully removable. As particles created here pass through the entire inner detector the vertex resolution is optimal.

Region 2 $0.9 \text{ cm} < dr \leq 16 \text{ cm}$: Here the vertex location is somewhere in the VXD, meaning good vertex resolution but increased backgrounds due to material interactions. This is demonstrated in Figure 4.4 as the peaks in the vertex distribution correspond to locations of high material density, especially the beam-pipe and SVD strips.

Region 3 $16 \text{ cm} < dr \leq 112 \text{ cm}$: The vertex location in this region is within the CDC, allowing for good vertex reconstruction with low passive material. The limiting factor is that, due to the L1 Trigger requirement of one 3D track as described in Chapter 2, any particles created beyond approximately 60 cm do not pass through sufficient drift chamber stereo layers to trigger and store the event.

Region 4 $112 \text{ cm} < dr$: Here the vertex is outside the CDC in a location covered by the ECL or KLM, so no accurate vertex reconstruction can be expected and the region is not included in any further analysis.

For the background studies the, at the time most, recent Monte Carlo (MC) sample produced by the Belle II data production team was used (MC13ria). This sample is run-independent, meaning it uses overlaid simulated beam backgrounds and static detector conditions. Statistics of the sample are equivalent to between 1 and 5 ab^{-1} of events and included the following channels:

- $e^+e^- \rightarrow u\bar{u}, e^+e^- \rightarrow d\bar{d}$
- $e^+e^- \rightarrow c\bar{c}, e^+e^- \rightarrow s\bar{s}$
- $e^+e^- \rightarrow \mu^+\mu^-, e^+e^- \rightarrow \tau^+\tau^-$
- $e^+e^- \rightarrow \pi^+\pi^-, e^+e^- \rightarrow K^+K^-$

In the subsequent analysis the four hadronic samples are shown together without differentiating between them individually. Figures 4.3 - 4.5 show the distributions of vertex location for the three most prominent backgrounds as well as example signal samples for a ρ_d^0 with mass $0.8 \text{ GeV}/c^2$ and average $c\tau$ of 0.25 and 10 cm respectively. After becoming available the selection criteria was tested again on the new MC15rib sample and was found to reduce the background to zero.

4.3 Background Separation

The dark sector in this model has, dependent on the exact choice of parameters, a very small coupling to the SM which makes it imperative to lose as little signal as possible while removing all of the background. Though it might be possible to leave a portion of the background and look for a signal peak on top of a smooth background distribution, the small magnitude of the signal peak could easily be drowned out by small fluctuations in the background.

This is complicated by the large available parameter space for the model. The most important parameter is the range of possible lifetimes, from essentially prompt decays to an average $c\tau$ of a few meters. Naturally, either extreme is hard to account for as a too short lifetime will not result in sufficiently displaced vertices

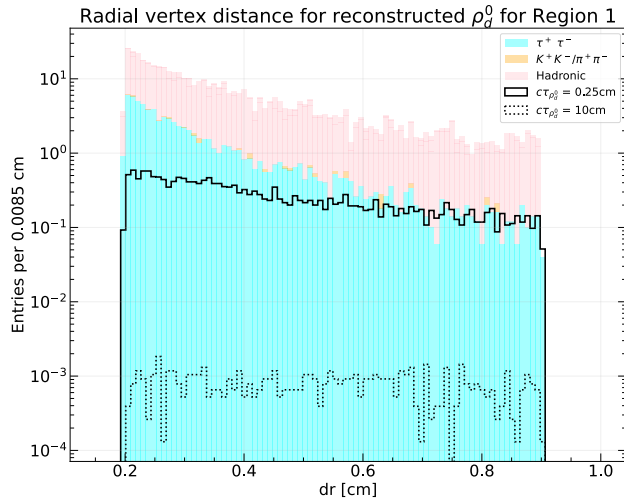


Figure 4.3: Backgrounds for vertex location $< 0.9\text{cm}$ after pre-selection. Black lines show example signal distributions for a ρ_d^0 with mass $0.8\text{ GeV}/c^2$ and two different average lifetimes.

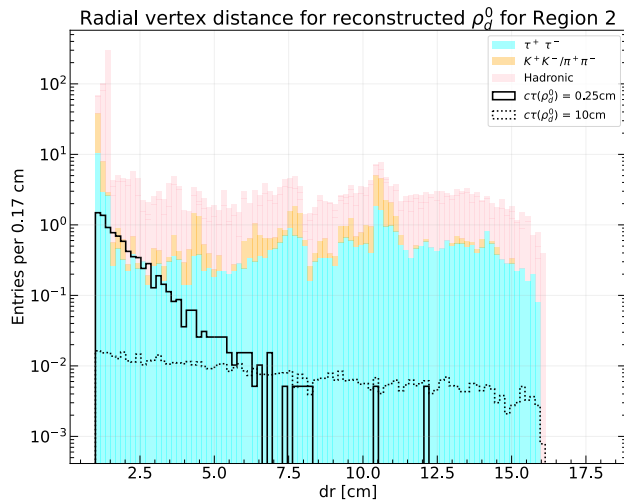


Figure 4.4: Backgrounds for vertex location $0.9 < dr \leq 16\text{cm}$ after pre-selection. Note the jagged structure corresponds to the radial material distribution in the detector

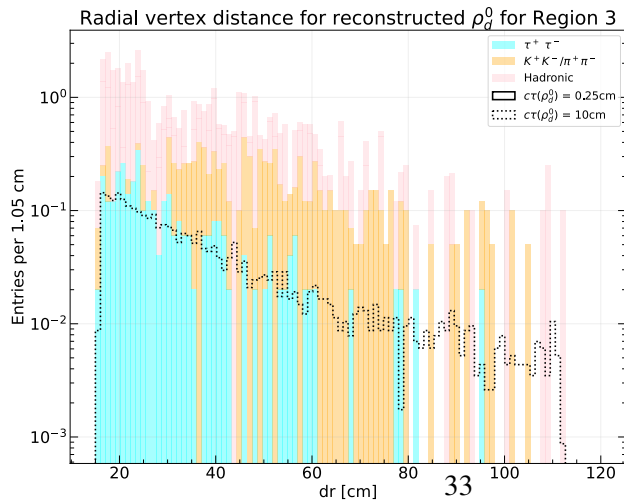


Figure 4.5: Backgrounds for vertex location $16 < dr \leq 120\text{cm}$ after pre-selection. Note the absence of signal for the shorter lived ρ_d^0 .

while an extremely long lifetime means the ρ_d^0 decays in a region where the tracks cannot be reconstructed or outside the detector entirely. The range in possible ρ_d^0 masses not only results in different kinematic distributions for the reconstructed LLP and its daughter muons, it also changes the ρ_d^0 multiplicity per event and affects the exact branching ratio to final state SM particles.

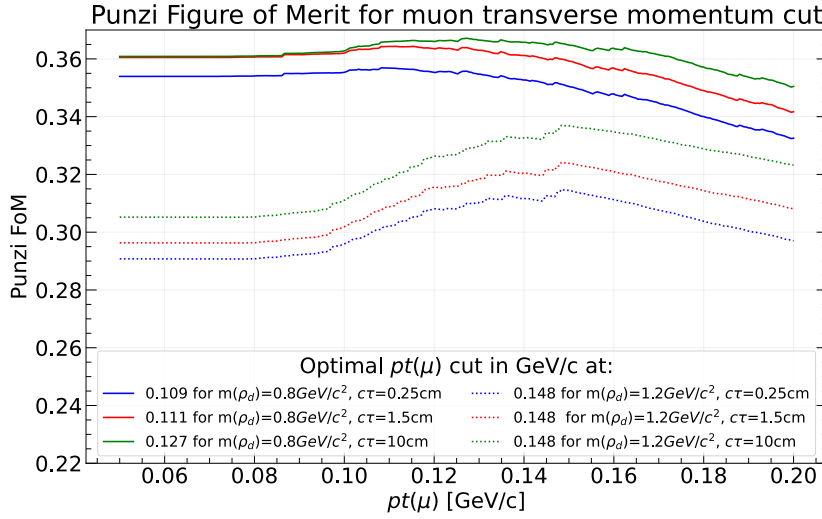


Figure 4.6: Example plot of the figure of merit, defined as number of signal events over number of remaining background events in a 400 MeV/c² range after 1 cut is applied. Specifically for the cut location on the daughter muon transverse momentum.

In light of this it was decided that simple rectangular cuts would be used instead of a complicated system of correlated cuts that would be more suitable for a smaller, more specific parameter space. These cuts were loosely optimized using a Punzi figure of merit, with a simple 1D scan over possible cut locations for a selection of valid combinations of mass and $c\tau$. The figure of merit is defined as the number of signal events after cuts divided by the number of remaining background events in a 400 MeV/c² range centered around the generated ρ_d^0 mass. Since the optimal cut location is slightly different for each set of parameters, a median value was chosen in each case, with cuts in Region 1 being optimized towards shorter

average lifetimes while the further regions were geared towards higher efficiencies for longer lived ρ_d^0 . The nonlinear nature of the figure of merit is shown in Figure 4.6. The overall signal cut efficiency is shown in Figure 4.7, one plot showing the efficiency compared to all generated events in the barrel while the other takes into account that the dark rho multiplicity is mass dependent and the fraction of events containing exactly one dark rho can be as low as 5% at low masses. Unsurprisingly the efficiency is best for the median range of average lifetimes between 1 and 10 cm. Since the production cross-section for lighter ρ_d^0 is significantly higher at lower masses, the considerably low signal efficiency below $0.4 \text{ GeV}/c^2$ was deemed acceptable. The exact selection criteria are detailed in the next section. The overall selection criteria, i.e. the cuts applied regardless of vertex location, is given in Table ??, while the region specific cuts are listed in Table ??.

4.4 Discriminating Variables

varibs There are a multitude of useful discriminating variables that can be used to separate signal from background.

- nTracks: Since the goal is to reconstruct events with a single ρ_d^0 we can reject all events with a track multiplicity higher than two.
- muonID: In The Belle II framework the muonID is the identification probability defined as the relative likelihood i.e. $L_\mu / (L_e + L_\mu + L_\pi + L_K + L_p)$, using information from all subdetectors. This variable is especially important as the background contribution from misidentified pions was significantly larger than initially expected. Additionally misidentification coupled with the high branching fraction to pions for low ρ_d^0 results in an additional peak when reconstruction the muon signal as shown in Figure 4.9. The distribution for muonID in two analysis regions is shown in Figure ??, where the large number of entries with low muonID for the example signal is due to both, the signal event containing misidentified pions and correctly identified muons with a low ID score due to not reaching the KLM.
- nPions: We attempt to reconstruct any π^0 and reject an event if it contains one or more, since it could only come from a ρ_d^0 decaying to 3 or more pions

or from background events.

- **Momentum–Vertex angle:** This is the angle between the reconstructed momentum vector of the ρ_d^0 and the vector formed by connecting its vertex location with the IP. Since the two decay products of the ρ_d^0 should reconstruct the momentum vector perfectly and the path of the ρ_d^0 is a straight line, this angle is expected to be (very close to) zero. The distribution in two regions is shown in Figure ??.
- **Helicity Angle η :** The Helicity Angle η is the angle between the line defined by the momentum difference of the muons in the ρ_d^0 rest frame and the ρ_d^0 momentum vector in the lab frame. This distribution peaks strongly at ± 1 for QCD background as the photon is massless while our massive ρ_d^0 has additional degrees as freedom and subsequently has a more flat distribution, as demonstrated by Figure ??.

Variable	θ	nTracks	Mass	pt(ρ_d^0)	pt(μ)
Value	31 - 128	==2	>0.5 or <0.4	>0.1	>0.1

Table 4.1: The overall selection criteria applied to every event. The θ range is such that the event is in the barrel and therefore excludes the end-caps which experience higher background levels. Mass in GeV/c^2 and momentum in GeV/c .

Variable	nPions	muonID	Significance of Distance	$ \cos(\eta) $	cos(PV)	Missing Energy
in Region 1	=0	>0.9	15	<0.8	>0.998	6
in Region 2	=0	>0.9	-	<0.8	>0.999	5
in Region 3	≤ 1	>0.99	-	<0.9	>0.9999	5

Table 4.2: Selection criteria dependent on vertex location. The three regions correspond to inside the beam-pipe, inside the inner detector and inside the CDC respectively. Missing Energy in GeV.

4.5 Trigger Efficiency

In the previous analysis it was assumed that the trigger efficiency for displaced vertices is close to 100%. In this section we will take a closer look at the currently implemented hardware and software triggers and their efficiencies. Naturally, different final states will benefit from different specific trigger configurations, but we can still make predictions for non-muon final states. In the detailed breakdown below we are only considering triggers that are not pre-scaled, meaning that if the trigger condition is met then the event is kept 100% of the time. Triggers that have a signal high efficiency, like the single muon trigger for example, do allow most signal events to pass but due to pre-scaling only keep every tenth event. Due to the low expected number of signal events these triggers were deemed as likely not contributing significantly to the overall triggering efficiency. It is implied that in addition to the requirements listed below each triggering event needs to not be rejected due to independent veto conditions. For Level 1 the most important triggers are:

STT Requires one Neuro track with momentum $> 0.7 \text{ GeV}/c$

STTECL Same as STT requirements plus one ECL cluster matched to a CDC track.

CDCKLM1(2) Requires one (two) KLM clusters matched to a CDC track.

FY30 Requires two 2D tracks, one of which is a Neuro track, and an opening angle larger than 30 degrees.

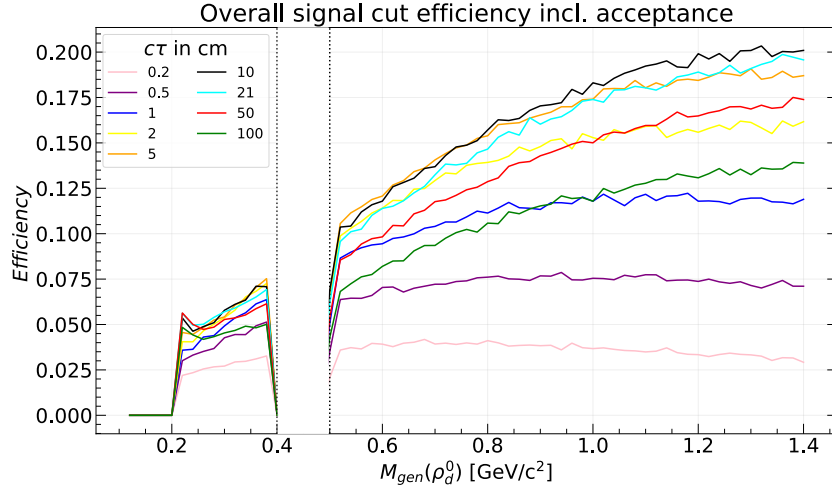
FYO Requires two 2D tracks, one of which is a Neuro track, and a CDC opening angle greater than 90 degrees.

MUb2b Requires two back-to-back clusters in the KLM

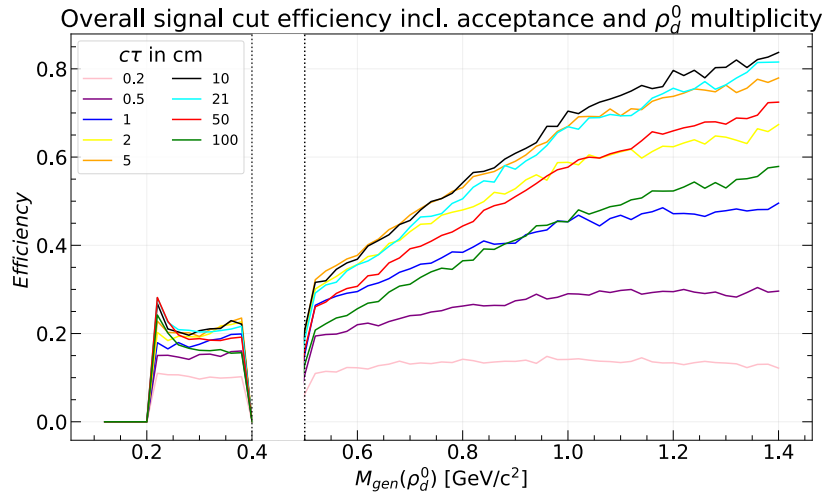
The individual efficiencies of each L1 trigger is shown in Figure 4.13a and Figure 4.13b. It is clear to see that the single track trigger (STT) is by far the most important triggering condition, followed by conditions requiring 2 tracks with either a matched KLM cluster or a large opening angle. Due to the minimum momentum requirement, the STT has highest efficiencies for higher ρ_d^0 masses. From Figure

4.12 it is apparent that L1 triggering efficiency is strongly lifetime dependent. As discussed in Chapter 2, a Neuro track requires the traversal of multiple stereo layers in the CDC, meaning a vertex location beyond ~ 60 cm is unlikely to fulfil this condition. The overall trigger efficiency at Level 1 is shown in Figure 4.12. For heavy ρ_d^0 we have very good ($>90\%$) efficiency for average lifetimes on the order of 20 cm, while for lighter ρ_d^0 the efficiency drops off steeply and only reaches around 50% for $c\tau > 10$ cm.

For the HLT there are fewer relevant triggers. The majority of events are triggered due to the “two loose tracks” requirement, with specifically the “2 loose tracks $0.8 < p_{\text{star}} < 4.5 \text{ GeV/c}$ ” trigger covering the majority of the events. As the name suggests, this requires two loose tracks, i.e. tracks with a momentum between 0.8 and 4.5 GeV/c. A loose track has the requirements of having the point-of-closest-approach of the track to be within 2 cm of the zero-point in the xy plane (d_0) and within 10 cm in z (z_0). The efficiency is lower for lighter dark rho as they tend to not fulfill the 0.8 GeV/c minimum momentum requirement. Most of the lower momentum dark rhos are instead covered by the “2 loose tracks inc 1 tight $q_{\text{star}} = 0$ $p_{\text{star}} < 0.8 \text{ GeV/c}$ ” trigger, which lacks the minimum momentum requirement but requires a higher quality of one of the two tracks. This complementary interaction also means that the HLT does not suffer from lower efficiency for lower ρ_d^0 masses. Similar to triggering at L1 we note that the efficiency drops significantly for high average lifetimes though not as dramatically, with Figure 4.14 showing that the efficiency is greater than 90% for average displacements of 10 cm, independent of ρ_d^0 mass. This is primarily due to the requirement of z_0 , as an extrapolated track resulting from the decay of a displaced particle is likely to be far from the IP. A proposed dedicated displaced vertex trigger, requiring a vertex between 0.9 and 60 cm in addition to minor kinematic requirements, will considerably improve the overall efficiency. The concern remains that sensitivity for larger lifetimes still requires the ρ_d^0 to decay in the first 60 cm.

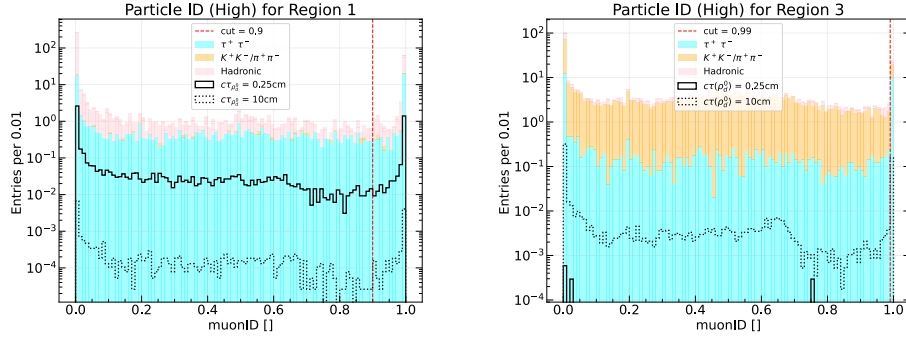


(a) Efficiency of the signal cuts compared to all generated events that are in the barrel of the detector.



(b) Efficiency of the selection cuts compared to all generated events in the barrel and containing a single ρ_d^0

Figure 4.7: Signal efficiency defined as the number of signal events after cuts divided by the number of generated events with muons in the final state. Note that the mass region from 0.4 to 0.5 GeV/c² is not plotted, corresponding to the signal selection cut to remove K_S^0 .



(a) muonID for the ρ_d^0 daughter with the higher ID value for $0.2 < dr \leq 0.9\text{cm}$

(b) muonID for the ρ_d^0 daughter with the higher ID value for $16 < dr \leq 112\text{cm}$

Figure 4.8: muonID score, defined as the relative likelihood including information from all subdetectors, for two different detector regions.

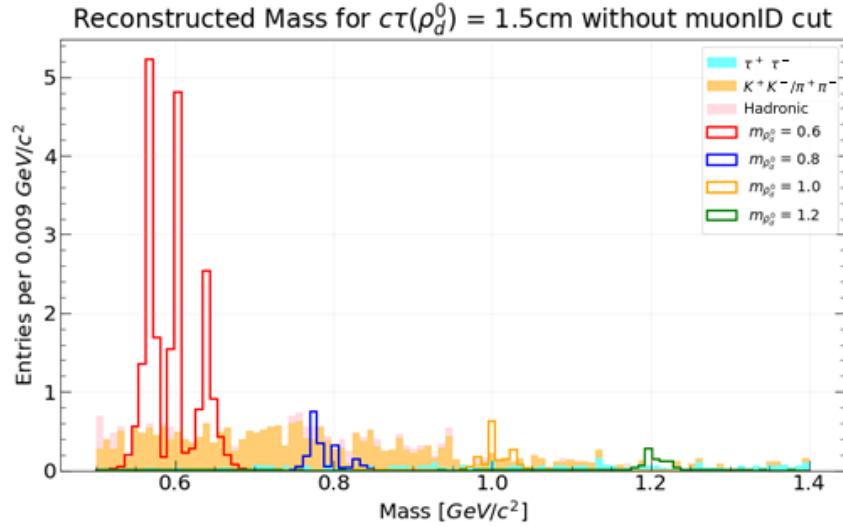
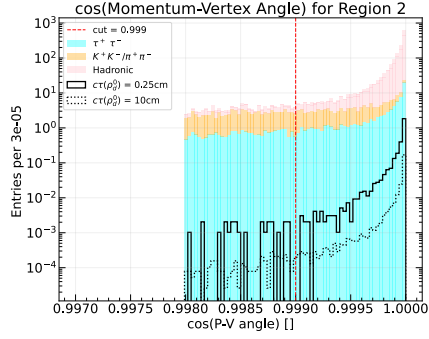
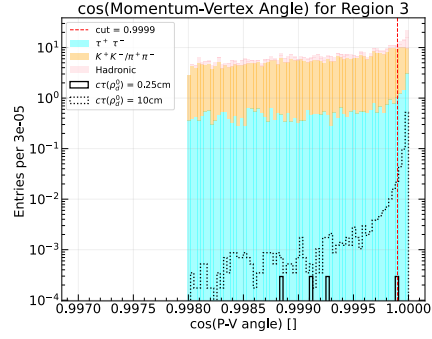


Figure 4.9: Reconstructed mass of signal and background, applying all selection cuts but no muonID cut. Note the large reflected peaks in red, blue, gold, and green due to misidentified pions.

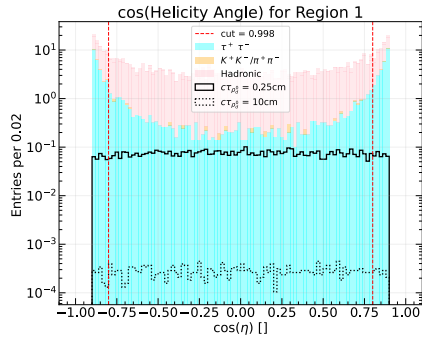


(a) Cosine of the momentum-vertex angle for $0.9 < dr \leq 16\text{cm}$

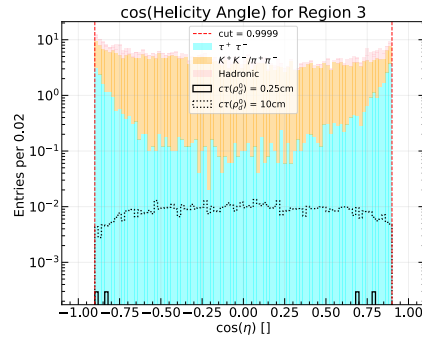


(b) Cosine of the momentum-vertex angle for $16 < dr \leq 112\text{cm}$

Figure 4.10: Cos(momentum-vertex angle) in two different regions. The combined momentum of the daughters should point in the same direction as the momentum of the mother for a 2 body decay, so the cosine of this angle is expected to be 1.



(a) Cosine of the helicity angle η for $0.2 < dr \leq 0.9\text{cm}$



(b) Cosine of the helicity angle η for $16 < dr \leq 112\text{cm}$

Figure 4.11: Cos(η) in two different detector regions. For our massive scalar particle this distribution is flat while the QCD background peaks strongly at plus/minus 1, due to the mediator of that interaction being the mass-less photon

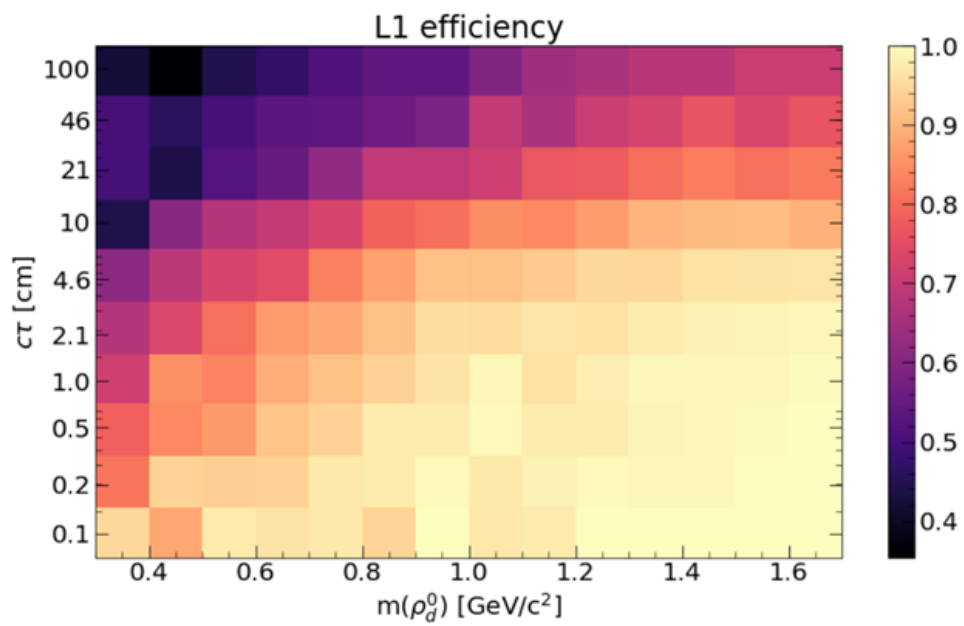
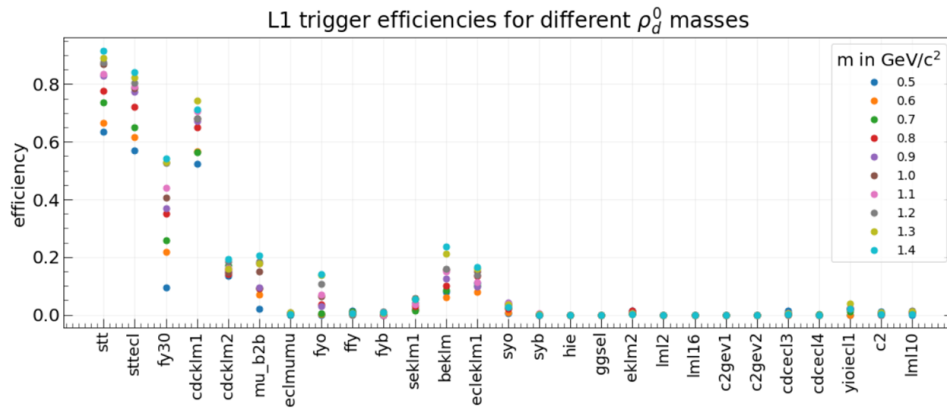
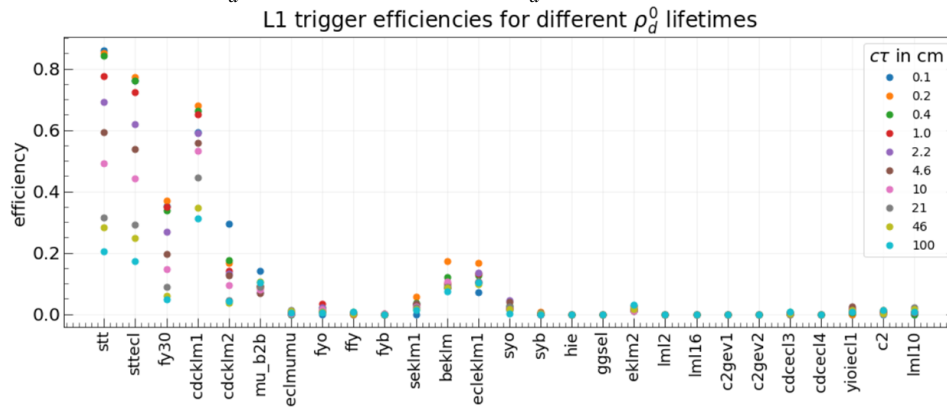


Figure 4.12: Overall efficiency of the L1 trigger



(a) ρ_d^0 Efficiencies for different ρ_d^0 masses with $c\tau \sim 5\text{cm}$



(b) Efficiencies for $m(\rho_d) = 0.8\text{GeV}/c^2$ and various average lifetimes

Figure 4.13: Level 1 trigger efficiencies for each unscaled trigger separately, both in terms of ρ_d^0 mass and lifetime.

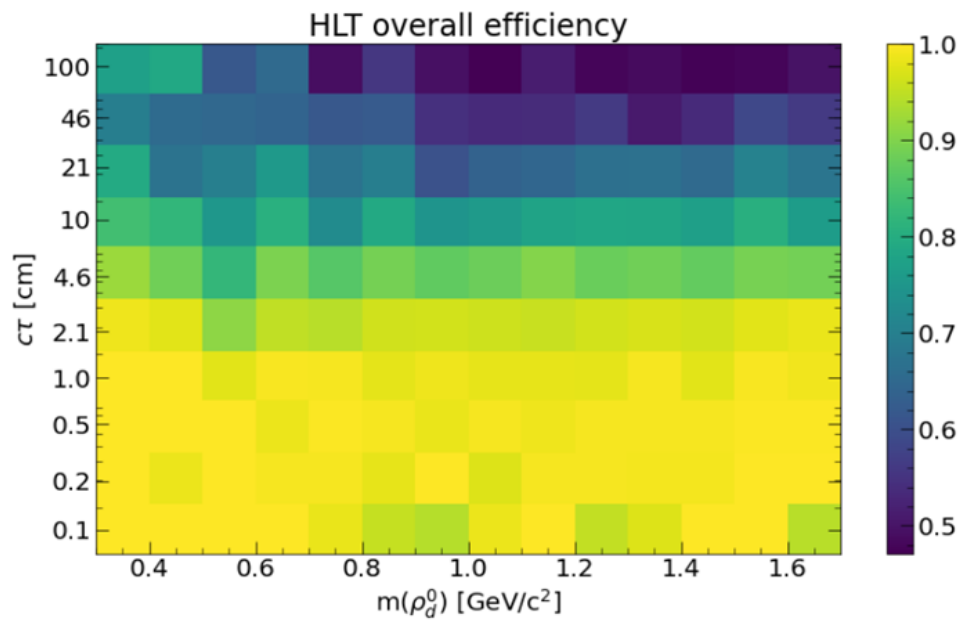


Figure 4.14: HLT efficiency after L1 Triggers have been applied.

Chapter 5

Analysis

To create the exclusion limits presented below, 50000 signal events were simulated for each parameter combination as described in Chapter 4. Specifically each point was generated with $m_{A'} = 20 \text{ GeV}/c^2$ and $\kappa = 0.014$, close to its maximal value, while the parameter e_d was varied such that the parameter combination resulted in a valid result for Λ . Other parameter combinations are certainly possible but as described in Chapter 3 the phenomenology can be fully discussed in terms of the effective interaction so that changing the parameters in such a way that the resulting value of Λ is the same would have no impact on the experimental signature. For the average lifetime it was sufficient to generate events at 13 different $c\tau$, from 0.1 cm to 1000 cm in logarithmic spacing. The background-less nature of the analysis and the high reconstruction precision for the signal results in a narrow mass peak, which coupled with the strong effect of QCD-resonances required a smaller (20 MeV/c^2), linear spacing in masses, with 60 different masses generate between 0.2 and 1.4 GeV/c^2 . While the model remains valid for ρ_d^0 masses of up to 2 GeV/c^2 , preliminary studies showed that the low production cross-section coupled with the low ρ_d^0 results insufficient sensitivity beyond $m(\rho_d^0) > 1.3 \text{ GeV}/c^2$, hence the chosen cutoff at 1.4 GeV/c^2 . The number of events after the selection criteria are applied is shown in Figure 5.1 while Figure 5.2 shows the number of events scaled to 500 fb^{-1} according to the MadGraph calculated cross-section.

The selected events were fit with a double-sided Crystal Ball function [26] using SciPy's *curve_fit*, which employs a least-squares fit with the trust region

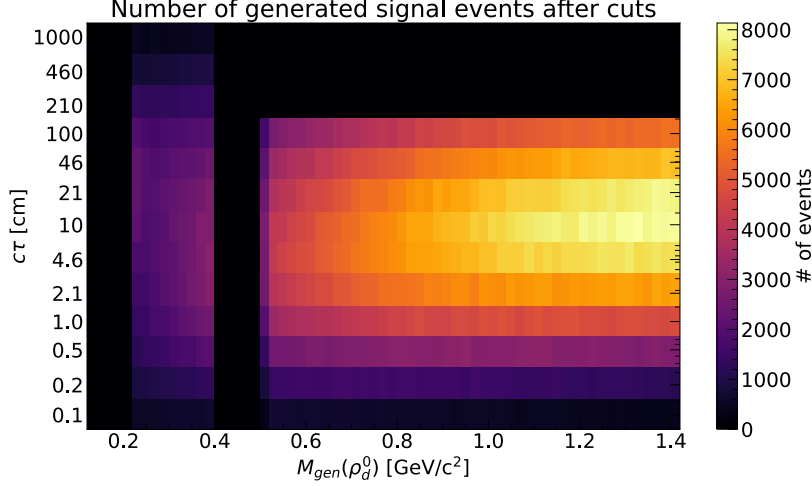


Figure 5.1: Number of events remaining from 50000 generated events after signal selection cuts are applied.

reflective (trf) method [28]. The fitting function is defined as:

$$f(x, \alpha_L, \alpha_R, \sigma, \mu, n) = \begin{cases} A_L \cdot (B_L - \frac{x-\mu}{\sigma})^{-n} & \text{for } \frac{x-\mu}{\sigma} < -\alpha_L \\ \exp\left(-\frac{(x-\mu)^2}{2\sigma^2}\right) & \text{for } -\alpha_L \leq \frac{x-\mu}{\sigma} \leq \alpha_R \\ A_R \cdot (B_R + \frac{x-\mu}{\sigma})^{-n} & \text{for } \frac{x-\mu}{\sigma} > \alpha_R \end{cases}$$

where:

$$A_{l/r} = \left(\frac{n}{|\alpha_{l/r}|}\right)^n \cdot \exp\left(-\frac{|\alpha_{l/r}|^2}{2}\right)$$

$$B_{l/r} = \frac{n}{|\alpha_{l/r}|} - |\alpha_{l/r}|$$

Since there is some ambiguity in the function between n , the power of the power law for each tail, and $\alpha_{L/R}$, the transition points between tail and core, it was decided to fix $n=3$ and only fit the remaining four parameters and an overall normalization. This also greatly increases the stability of the fit as small variations in the power have a great effect on the overall shape of the Crystal ball function, so fixing n to a constant value ensures all fits converge without failures. Six example fits are

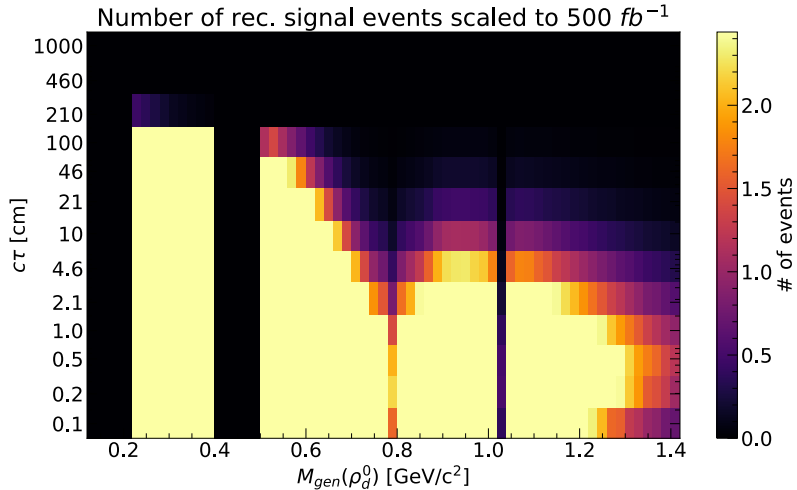


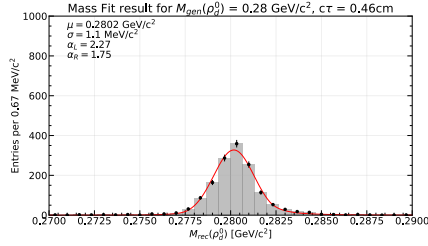
Figure 5.2: Number of events remaining from 50000 generated events after signal selection cuts and MadGraph calculated cross-section are applied, i.e. scaled to an equivalent of 500 fb^{-1} . The heatmap maximum corresponds to the number of events required to exclude a point in parameter space according to Feldmann-Cousins 90% confidence intervals.

shown in Figure 5.3. The fit results for the shape parameters and width is shown in Figure 5.7 and Figure 5.8 respectively.

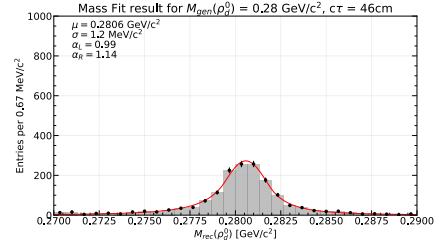
To gauge the goodness of fit we first calculate the reduced chi square: $\chi_{red}^2 = \chi^2/DoF$ where DoF is the number of degrees of freedom of the fit. The individual chi square values can be seen in Figure 5.4 but overall the fits are satisfactory with an average χ_{red}^2 of 1.36.

To gauge the quality of the reconstruction we can examine the mass uncertainty calculated by the reconstruction algorithm, shown below in Figure 5.5, as well as the mass pulls. Here the mass pulls are defined as $(M_{reconstructed} - M_{generated})/\sigma_M$ where σ_M is the uncertainty in reconstructed mass. These pulls are then fitted to a normal distribution with the resulting mean and standard deviations are shown in Figure 5.6. A slight positive bias can be observed, indicating that the reconstructed mass tends to be higher than the generated value.

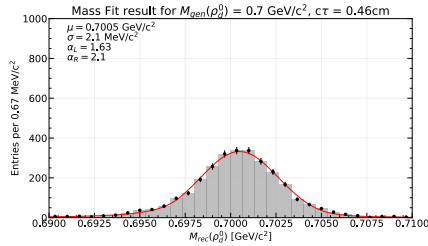
We can then construct 90% confidence level exclusion bounds by including all



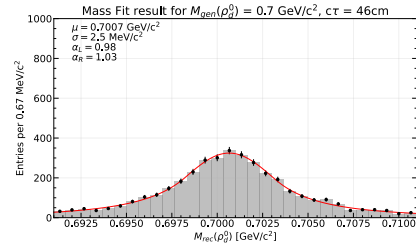
(a) Crystal Ball fit for $m(\rho_d)=0.28 \text{ GeV}/c^2$ with $c\tau=0.46 \text{ cm}$



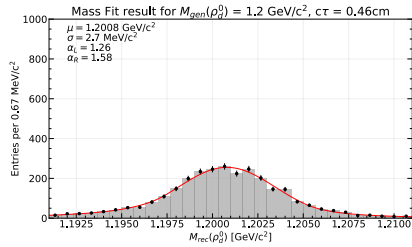
(b) Crystal Ball fit for $m(\rho_d)=0.28 \text{ GeV}/c^2$ with $c\tau=46 \text{ cm}$



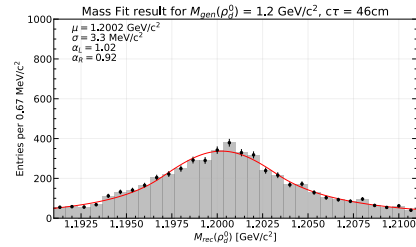
(c) Crystal Ball fit for $m(\rho_d)=0.70 \text{ GeV}/c^2$ with $c\tau=0.46 \text{ cm}$



(d) Crystal Ball fit for $m(\rho_d)=0.7 \text{ GeV}/c^2$ with $c\tau=46 \text{ cm}$



(e) Crystal Ball fit for $m(\rho_d)=1.20 \text{ GeV}/c^2$ with $c\tau=0.46 \text{ cm}$



(f) Crystal Ball fit for $m(\rho_d)=1.20 \text{ GeV}/c^2$ with $c\tau=46 \text{ cm}$

Figure 5.3: Double sided Crystal Ball fits for ρ_d^0 with a range of average lifetimes and masses using a fixed fitting range of $20 \text{ MeV}/c^2$. Note the increasing width with both mass and average displacement.

parameter combinations that predict more than 2.44 events. This value is the upper bound of the 90% confidence level interval for a Poisson signal mean as calculated by reference [13]. A plot of the projected exclusion bounds is shown in Figure 5.9.

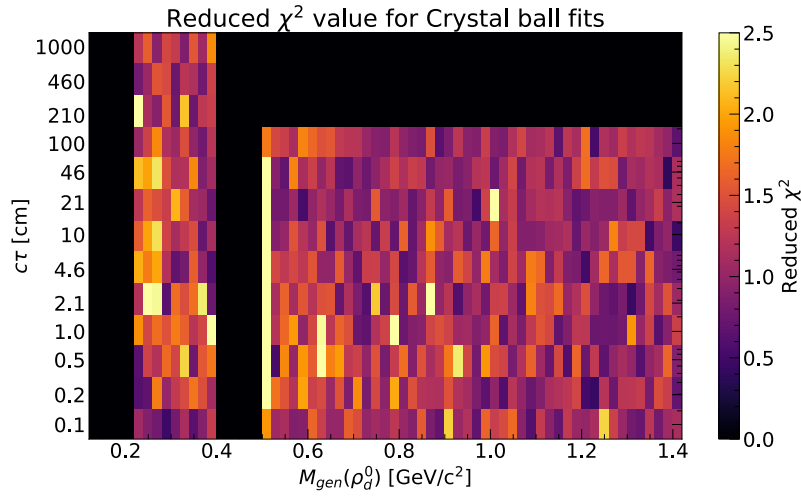


Figure 5.4: Reduced χ^2 values for each individual Crystal Ball fit.

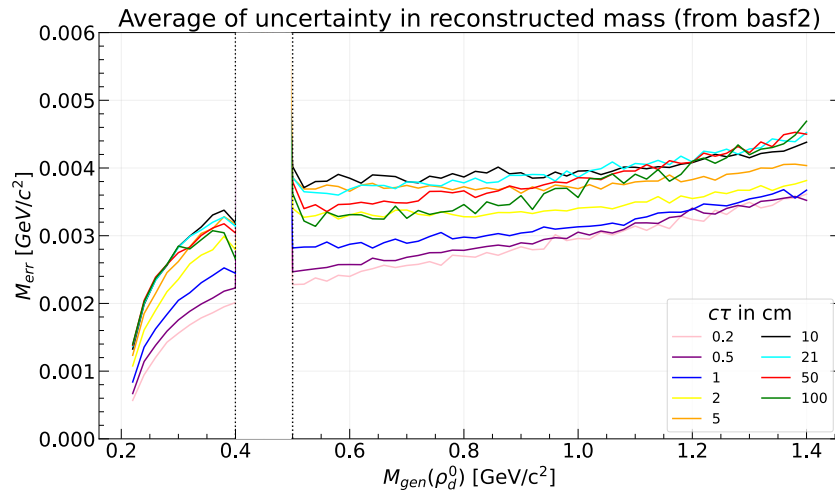
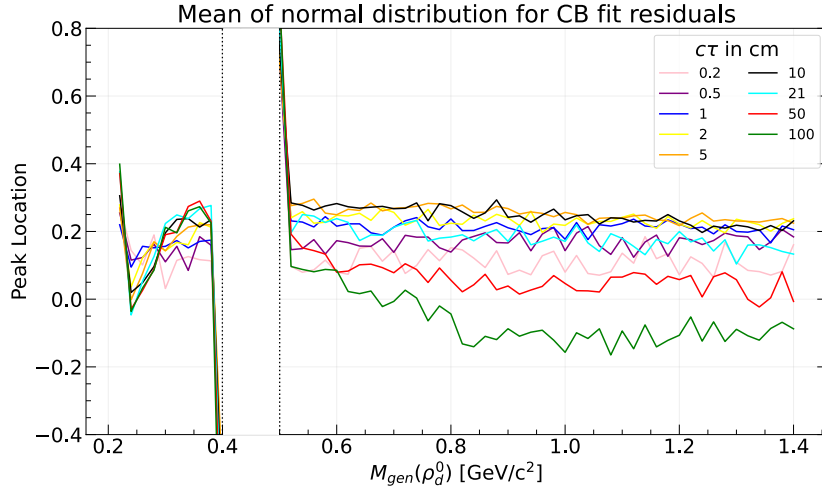
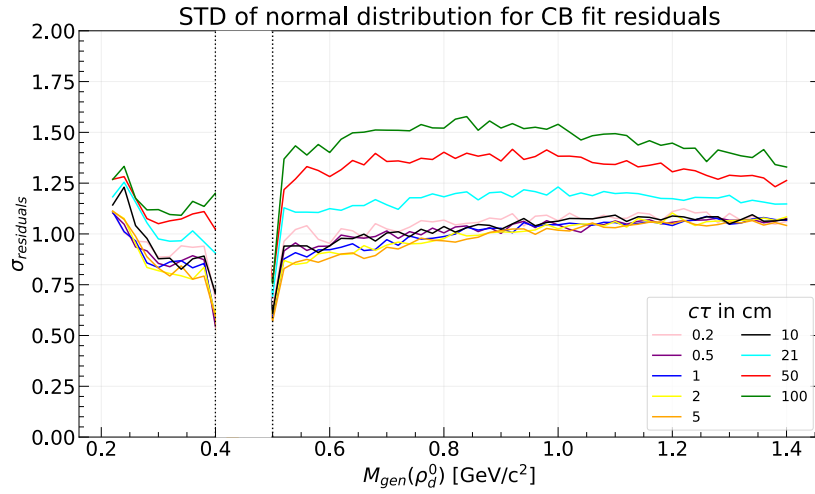


Figure 5.5: Uncertainty in the reconstructed mass as reported by the reconstruction algorithm.

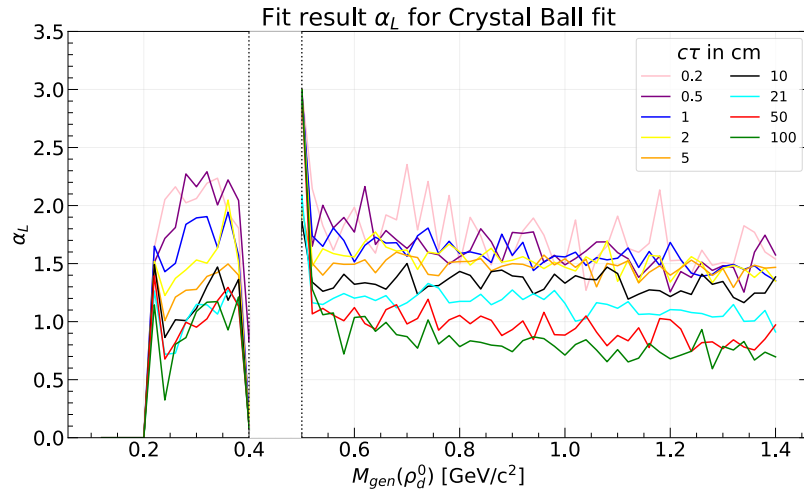


(a) Mean of the fitted residuals, expected to be 0. A slight positive bias can be observed indicating that the reconstructed mass is slightly higher than generated

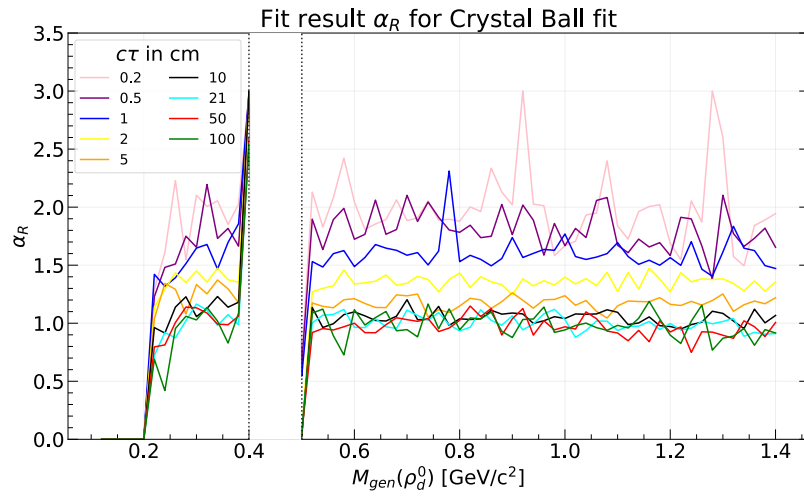


(b) Standard deviation of the fitted residuals, expected to be 1. Reconstructed ρ_d^0 with larger lifetimes have increasing spread in residuals.

Figure 5.6: Mean and std for mass pulls. Note that the parameter space from 0.4 - 0.5 GeV/c^2 contains almost no signal events, so any fit is expected to fail or produce extreme outliers in that region.

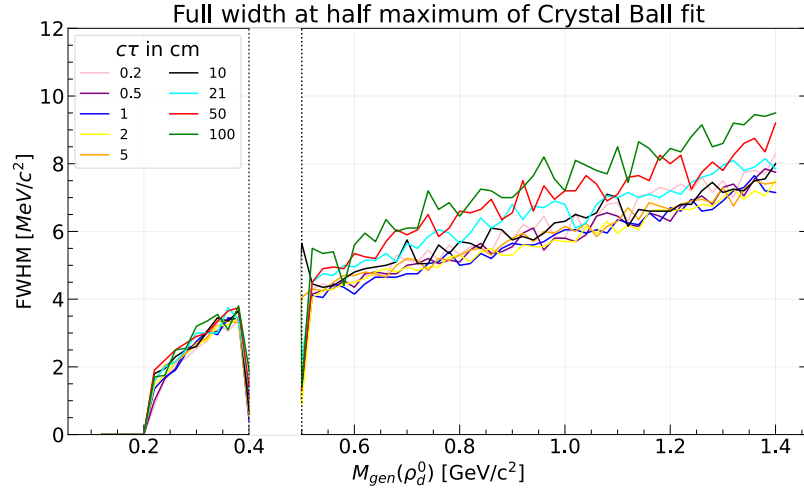


(a) Fit result for parameter α_L

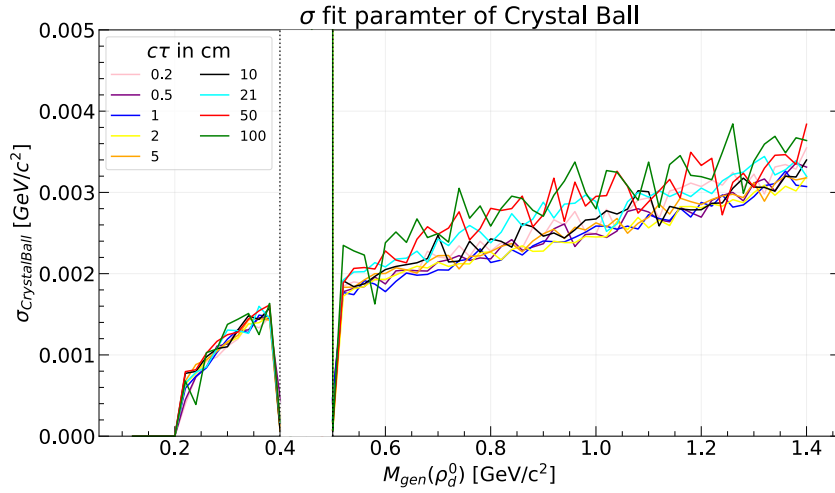


(b) Fit result for parameter α_R

Figure 5.7: Fit results for the shape parameter α , which determines the transition location of exponential tail to power law in the Crystal Ball function. The fit result is reasonably constant for a given average lifetime.



(a) Full width at half maximum for the Crystal Ball fit.



(b) Fit result for parameter σ which determines the width of the Gaussian core.

Figure 5.8: Two measures of the signal width, FWHM above and the width of the Gaussian core of the Crystal Ball function below. Since the wider signal samples can be dominated by the power law tails of the functions the FWHM is a better indicator of signal width than σ despite the similar distributions.

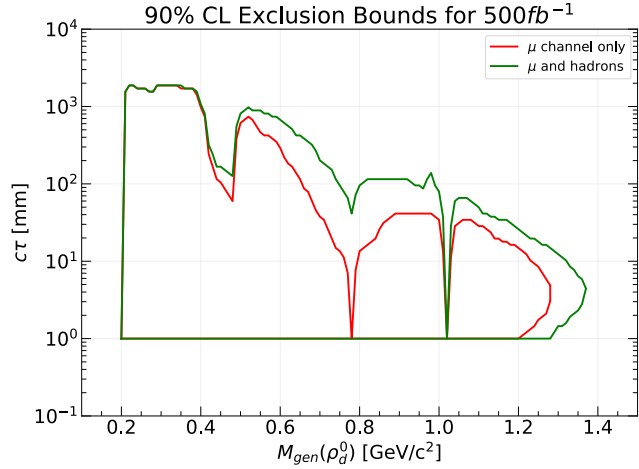


Figure 5.9: 90% Confidence Level exclusion bounds for mu channel (in red) and projection for combined mu and hadronic channel (in green). Note the large impact of QCD resonances, especially from ϕ and ω mesons

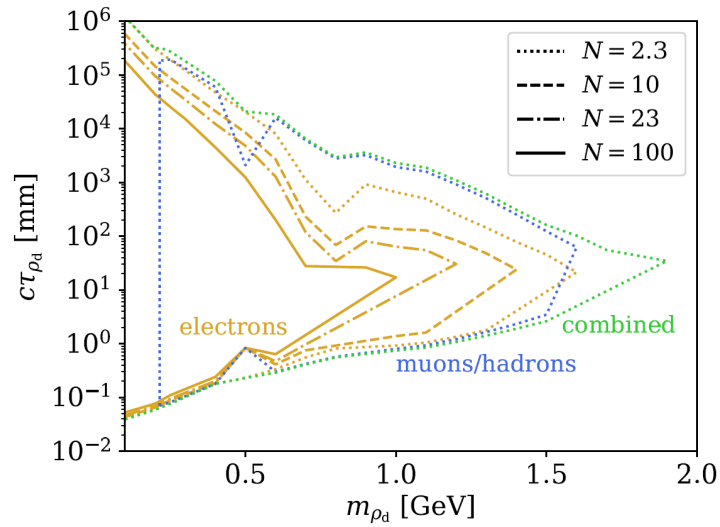


Figure 5.10: Exclusion bounds from Bernreuther et.al., assuming an implemented displaced vertex trigger and minimal backgrounds [8].

Chapter 6

Conclusion and Outlook

The goal of this thesis was to explore a model of a QCD-like dark sector and the resulting dark shower signature at Belle II. We investigated the feasibility of a zero-background analysis by focusing on events with a single LLP decaying to a pair of muons and found a combination of selection cuts that consistently reduce the background levels to zero. These criteria were tested with a large set of simulated MC backgrounds and a large variety of possible parameter combinations. The resulting 90% confidence level exclusion bounds are presented in Figure 5.9, showing both the bounds obtained for the muon signal as well as a projection if other hadronic final states were to be considered. In order to contextualize these exclusion bounds, we can compare them to bounds presented by reference [8], shown in Figure 5.10. In their paper, they recast BaBar results and compare them to the projected sensitivity at Belle II. Their Belle II projection includes all possible final states and ρ_d^0 multiplicities compared to the limit of a single ρ_d^0 decaying to a pair of muons presented in this thesis. Bernreuther et. al. further make the assumption that, with a yet-to-be-implemented displaced vertex trigger, the triggering efficiency will be close to 100% while full background suppression can be achieved with minimal cuts on momenta and opening angles in addition to a displaced vertex requirement. As we have shown in Chapter 4, the cuts required to reduce the background to zero lead to a significant loss in signal efficiency, with losses ranging from 15% for a heavier ρ_d^0 with a displacement on the order of centimeters, to as high as 85% signal loss for light ρ_d^0 with $c\tau$ larger than ~ 100 cm. Perhaps most impactful is the

problem of misidentified particles. As shown in Figure 4.9 the misidentification of pions causes secondary peaks in the signal, requiring a strong particle ID cut. For the lowest end of lifetimes, i.e. below $c\tau = 1$ mm, it is to be expected that most ρ_d^0 are not sufficiently displaced and events will not pass the $d_r > 0.2$ cm displaced vertex requirement. While some ρ_d^0 , even with a very low average lifetime, will certainly decay past 0.2 cm, the lower-than-expected signal efficiency severely limits Belle II's sensitivity in this region. Conversely, for extremely long average lifetimes, any retained event will require a vertex position in the CDC to pass trigger requirements. Here the low signal efficiency is similarly limiting as shown by the sharp cutoff after $c\tau > 1000$ mm in Figure 5.2. However, even limiting ourselves to events with 2 tracks and only considering muons and hadronic final states, it can be expected that Belle II can improve over existing constraints from BaBar with as little as 500 fb^{-1} of data. Furthermore, the planned displaced vertex triggers will provide a significant improvement in triggering rates, increasing Belle II's sensitivity even further. Reference [8] demonstrates that a similar displaced vertex search at LCHb will be primarily sensitive to higher masses and shorter lifetimes, making it perfectly complementary to possible analyses at Belle II. From this analysis it is clear that Belle II has excellent sensitivity to long lived particles with proper decay length between 0.1 and 60 cm. A zero-background analysis is feasible for muon and hadronic final states in the 2-track case, which can likely be extended to analyses with 4 tracks in the final state. We cannot make definite statements on analyses that involve electrons in the final state but the signal loss from the muon signature implies that a different approach, such as looking for a signal peak on top of a smooth background distribution, would need to be employed.

Bibliography

- [1] I. Adachi, T. Browder, P. Križan, S. Tanaka, and Y. Ushiroda. Detectors for extreme luminosity: Belle II. *Nucl. Instrum. Methods. Phys. Res. A*, 907: 46–59, 2018. ISSN 0168-9002. doi: <https://doi.org/10.1016/j.nima.2018.03.068>. → pages 13, 16, 60
- [2] N. Aghanim. Planck 2018 results. *Astronomy & Astrophysics*, 641:A6, 2020. doi: [10.1051/0004-6361/201833910](https://doi.org/10.1051/0004-6361/201833910). → page 3
- [3] S. Agostinelli et al. Geant4 — a simulation toolkit. *Nucl. Instrum. Methods. Phys. Res. A*, 506(3):250–303, 2003. ISSN 0168-9002. doi: [https://doi.org/10.1016/S0168-9002\(03\)01368-8](https://doi.org/10.1016/S0168-9002(03)01368-8). → page 17
- [4] A. Alloul et al. Feynrules2.0 — a complete toolbox for tree-level phenomenology. *Comp. Phys. Comm.*, 185(8):2250–2300, 2014. ISSN 0010-4655. doi: <https://doi.org/10.1016/j.cpc.2014.04.012>. → page 28
- [5] J. Alwall et al. MadGraph 5: going beyond. *Journal of High Energy Physics*, 2011(6), jun 2011. doi: [10.1007/jhep06\(2011\)128](https://doi.org/10.1007/jhep06(2011)128). → page 28
- [6] N. A. Bahcall. Cosmology with clusters of galaxies. *Phys. Scripta T*, 32, 2000. doi: [10.1238/Physica.Topical.085a00032](https://doi.org/10.1238/Physica.Topical.085a00032). → page 2
- [7] E. Bernreuther. *Accelerator phenomenology of strongly interacting dark sectors*. PhD thesis, RWTH Aachen U., 2021. → pages 21, 26, 27, 28
- [8] E. Bernreuther et al. Forecasting dark showers at belle II, 2022. → pages 53, 54, 55
- [9] D. Clowe. A direct empirical proof of the existence of dark matter. *Astrophys. J. Lett.*, 109, 2006. doi: [10.1086/508162](https://doi.org/10.1086/508162). → page 3
- [10] I. N. di Fisica Nucleare. Silicon vertex detector. URL <https://web.infn.it/Belle-II/index.php/detector/svd>. → page 12

- [11] S. Dodelson. The real problem with MOND. *Int. J. Mod. Phys. D*, 20(14): 2749–2753, dec 2011. doi: 10.1142/s0218271811020561. → page 4
- [12] M. Duerr et al. Invisible and displaced dark matter signatures at belle II. *Journal of High Energy Physics*, 2020(2), feb 2020. doi: 10.1007/jhep02(2020)039. → page 31
- [13] G. J. Feldman and R. D. Cousins. Unified approach to the classical statistical analysis of small signals. *Physical Review D*, 57(7):3873–3889, apr 1998. doi: 10.1103/physrevd.57.3873. → page 48
- [14] R. Itoh et al. The performance of Belle II high level trigger in the first physics run. *EPJ Web Conf.*, 245:01040, 2020. doi: 10.1051/epjconf/202024501040. → page 20
- [15] Y. Iwasaki et al. Level 1 trigger system for the Belle II experiment. In *2010 17th IEEE-NPSS Real Time Conference*, pages 1–9, 2010. doi: 10.1109/RTC.2010.5750454. → page 19
- [16] C. Kiesling et al. A neural network on FPGAs for the z-vertex track trigger in belle II. *Journal of Instrumentation*, 12(03):C03065–C03065, mar 2017. doi: 10.1088/1748-0221/12/03/c03065. → page 19
- [17] S. Knapen, J. Shelton, and D. Xu. Perturbative benchmark models for a dark shower search program. *Physical Review D*, 103(11), jun 2021. doi: 10.1103/physrevd.103.115013. → page 29
- [18] E. Kou et al. The belle II physics book. *Progress of Theoretical and Experimental Physics*, 2019(12), dec 2019. doi: 10.1093/ptep/ptz106. → page 8
- [19] T. Kuhr. The Belle II core software. *Comput. Softw. Big Sci.*, 2019. doi: https://doi.org/10.1007/s41781-018-0017-9. → page 17
- [20] S. Lee, R. Itoh, N. Katayama, and S. Mineo. Development of high level trigger software for belle II at SuperKEKB. *Journal of Physics: Conference Series*, 331(2):022015, dec 2011. doi: 10.1088/1742-6596/331/2/022015. → page 19
- [21] K. Olive. Review of particle physics. *Chinese Physics C*, 40(10):100001, oct 2016. doi: 10.1088/1674-1137/40/10/100001. → page 4
- [22] M. Roos. Dark matter: The evidence from astronomy, astrophysics and cosmology, 2010. → page 2

- [23] V. C. Rubin and W. K. Ford. Rotation of the andromeda nebula from a spectroscopic survey of emission regions. *Astrophys. Journal*, 379, 1970. doi: 10.1086/150317. → page 2
- [24] S. Sandilya. Particle identification at belle II. *J. Phys. Conf. Ser.*, 770: 012045, nov 2016. doi: 10.1088/1742-6596/770/1/012045. → page 14
- [25] T. Sjöstrand et al. A comprehensive guide to the physics and usage of pythia 8.3, 2022. → page 28
- [26] T. Skwarnicki. *A study of the radiative CASCADE transitions between the Upsilon-Prime and Upsilon resonances*. PhD thesis, Cracow, INP, 1986. → page 45
- [27] M. Srebre et al. Generation of Belle II pixel detector background data with a gan. *EPJ Web of Conferences*, 245:02010, 01 2020. doi: 10.1051/epjconf/202024502010. → page 10
- [28] P. Virtanen et al. SciPy 1.0: Fundamental Algorithms for Scientific Computing in Python. *Nature Methods*, 17:261–272, 2020. doi: 10.1038/s41592-019-0686-2. → page 46
- [29] X-ray: NASA/CXC/CfA/M.Markevitch et al.; Optical: NASA/STScI; Magellan/U.Arizona/D.Clowe et al.; Lensing Map: NASA/STScI; ESO WFI . Chandra image of the bullet cluster, 2013. [Online; accessed September 16, 2022]. → page 3
- [30] F. Zwicky. Die Rotverschiebung von extragalaktischen Nebeln. *Helv. Phys. Acta*, 110, 1933. doi: 10.1007/s10714-008-0707-4. → page 2

Appendix A

Appendix

Purpose	Name	Component	Configuration	Readout Channels	θ coverage
Beam pip		Beryllium	Cylindrical, inner radius 10 mm, 10 μ m Au, 0.6 mm Be, 1 mm paraffin, 0.4 mm Be		
Tracking	PXD	Silicon Pixel (DEPFET)	Two layers at radii 14 mm and 22 mm Sensor size by layer: $12.5 \times (L1\ 44.8, L2\ 61.44)\ mm^2$ Pixel size by layer: $50 \times (L1a/b\ 55/60, L2a/b\ 70/85)\ \mu m^2$	7.7M	[17°; 150°]
	SVD	Silicon Strip (double sided)	Rectangular and trapezoidal sensors strip pitch: $50(p)/160(n)-75(p)/240(n)\ \mu m$	245k	[17°; 150°]
	CDC	Drift Chamber	Four layers at radii: 39, 80, 104, 135 mm small cell, large cell, 56 layers	14k	[17°; 150°]
Particle ID	TOP	Quartz radiator	Barrel: 16 segments in ϕ at $\sim 120cm$, 275 cm long, 2 cm thick quartz bars with 4×4 channel MCP PMTs	8k	[31°; 128°]
	ARICH	Aerogel radiator	FWD end-cap: 2×2 cm thick focusing radiators with different η , HAPD photodetectors	60k	[15°; 34°]
Calorimetry	ECL	CsI(Tl)	Barrel: $r=125\ 162$ cm End-caps: at $z = 102$ cm and $z = +196$ cm	6624 (Barrel) 1152 (FWD) 960 (BWD)	[12.4°; 31.4°], [32.2°; 128.7°], [130.7°; 155.1°]
Muon ID	KLM	Barrel: RPCs and scintillator strips	2 layers with scintillator strips and 13 layers with 2 RPCs	16k in θ 16k in ϕ	[40°; 129°]
	KLM	End-caps: scintillator strips	14 (12) layers of $[7-10] \times 40\ mm^2$ strips in forward (backward) region	17k	[25°; 40°], [129°; 155°]

Table A.1: Summary of the Belle II detector components. FWD and BWD stand for forward and backward end-caps [1].